FY22 National Laser Users' Facility Program

M. S. Wei

Laboratory for Laser Energetics, University of Rochester

The Office of Experimental Sciences of the National Nuclear Security Administration within the U.S. Department of Energy funds the operations of LLE and specifically, of the National Laser Users' Facility (NLUF), thus making it possible for users from universities and industry in the United States to conduct basic science experiments without a direct facility charge. To better serve a growing, diverse user community and streamline the process, the NLUF Program has evolved into a facility-access-only program starting from FY22. During FY21, LLE completed a call for proposals, review, and selection process for the NLUF experiments to be conducted at the Omega Laser Facility during FY22 and FY23. After peer review by an independent proposal review panel for scientific merit and broad impact and the feasibility and executability review by the Omega facility and experimental support team, LLE selected 27 proposals for Omega shot allocation with a total of 25.5 and 34 shot days for experiments in FY22 (Q2–Q4) and FY23, respectively.

FY22 was the first of a two-year period of performance for these 27 NLUF projects (Table I). In addition, a few FY21 NLUF projects as carryover also completed experiments during FY22. In total, 314 target shots were conducted for NLUF projects during FY22. The NLUF experiments conducted during FY22 are summarized in this section.

Table I: Four FY21 carryover projects (in gray) conducted shots during FY22. Twenty-one (in blue) of the 27 new NLUF projects approved for the FY22–FY23 Omega Laser shot allocation conducted shots during FY22. The remaining six (in yellow) are scheduled for FY23.

Principal Investigator	Institution	NLUF Project Title/Article Title
F. N. Beg	University of California, San Diego	Charged-Particle Transport and Energy Deposition in Warm Dense Matter with and without an External Magnetic Field/ Measurements of Temperature Evolution in Copper from Intense Proton Beam Energy Deposition
W. Fox	Princeton University	Magnetic Reconnection in High-Energy-Density Plasmas
H. Ji/L. Gao	Princeton University/Princeton Plasma Physics Laboratory	Study of Particle Acceleration from Magnetically Driven Collisionless Reconnection at Low Plasma Beta Using Laser-Powered Capacitor Coils/Electron Exhaust Jets and Current-Driven Kinetic Instabilities in Laser-Powered Magnetic Reconnection
C. K. Li	Massachusetts Institute of Technology	Inertial Confinement Fusion Interface
M. Bailly-Grandvaux	University of California, San Diego	Effects of an External Magnetic Field on Laser–Plasma Instabilities
T. Duffy	Princeton University	Dynamic Compression of Exoplanetary Materials: Pressure-Induced B1–B2 Phase Transition in ZnO Under Laser-Driven Ramp Compression

Table I: Four FY21 carryover projects (in gray) conducted shots during FY22. Twenty-one (in blue) of the 27 new NLUF projects approved for the FY22–FY23 Omega Laser shot allocation conducted shots during FY22. The remaining six (in yellow) are scheduled for FY23 (continued).

Principal Investigator	Institution	Title
J. A. Frenje	Massachusetts Institute of Technology	Advanced Studies of Kinetic and Multi-Ion-Fluid Effects, Electron-Heat Conduction, Ion–Electron Equilibration, and Ion-Stopping Power in High-Energy-Density Plasmas/Multi-Ion Campaign: Studies of Multi-Ion and Kinetic Effcts in Shock and Ablatively Driven Implosions
M. Gatu Johnson	Massachusetts Institute of Technology	Study of Diffusion, Interpenetration, Instability, and Dynamics at the Ablator–Gas Interface in Inertial Confinement Fusion-Relevant Conditions/Ablator–Gas Interface Dynamics and Mix in Confinement Fusion-Relevant Conditions
R. Jeanloz/G. Tabak	University of California, Berkeley/LLE	Search for Immiscibility in Hydrogen–Neon Mixtures at Jupiter-Interior Conditions/Report for DACPlanet-22A/B
K. Krushelnick	University of Michigan	The Dynamics and Reconnection of Strong Magnetic Fields Using OMEGA EP/Plasmoid Magnetic Reconnection Between Long-Pulse Laser-Driven Plasmas Perturbed by a Short-Pulse Laser
C. C. Kuranz/ H. LeFevre	University of Michigan	Radiation Transport in Strongly Coupled Plasmas/Achieving Neutron Star Envelope Relevant Conditions Through a Radiative Shock in Strongly Coupled Plasmas
C. C. Kuranz/ H. LeFevre	University of Michigan	Photoionization Fronts on the OMEGA Laser/Observation of a Radiative Heat Front in Ar Using the Omega Gas-Jet System
D. Lamb/P. Tzeferacos	University of Chicago/ LLE	Onset, Subsistence, and Decay of Magnetized Turbulence and Fluctuation Dynamo
E. Liang	Rice University	Collision of Magnetized Jets Created by Hollow-Ring Lasers Irradiating High-*Z*–Doped CH Targets
R. C. Mancini	University of Nevada, Reno	X-Ray Heating and Ionization of Photoionized Plasmas in a Steady State
W. L. Mao	Stanford University	Low-Entropy Diamond Formation Pathways for Reactive H Chemistry/Shock-Induced Hydrogen Chemistry for Hydride Formation
C. McGuffey	General Atomics	Opacity of Ionized Iron Under Broad Pressure and Temperature Conditions/Driving Iron to Dense, Hot Conditions Using the Long- and Short-Pulse Beams of OMEGA EP
J. Shang	University of Rochester	Tracking Rarefaction with Particle Image Velocimetry
B. Srinivasan	Virginia Tech	Rayleigh–Taylor Evolution of Isoloated-Feature Perturbations in a Background Magnetic Field
S. Tochitsky/N. Lemos	University of California, Los Angeles/LLNL	Control of Laser–Plasma Interactions in Three-Dimensional–Printed Foam Structures with Graded Density
S. J. Tracy	Carnegie Institute for Science	Dynamic Compression of Iron Carbide at Exoplanetary Core Conditions

Table I: Four FY21 carryover projects (in gray) conducted shots during FY22. Twenty-one (in blue) of the 27 new NLUF projects approved for the FY22–FY23 Omega Laser shot allocation conducted shots during FY22. The remaining six (in yellow) are scheduled for FY23 (continued).

Principal Investigator	Institution	Title
P. Valdivia	University of California, San Diego/Johns Hopkins University	Phase-Contrast Imaging of Inner Shell Release Through Talbot–Lau X-Ray Interferometry/Monochromatic Talbot–Lau X-Ray Deflectometer for the OMEGA EP and Multi-Terawatt Lasers
T. White	University of Nevada, Reno	Experimental Measurement of Thermal Conductivity in Warm Dense Matter
J. Wicks	Johns Hopkins University	Exploration of Decomposition Kinetics in the Warm-Dense-Matter Regime: Orientation and Melting Effects
L. Willingale	University of Michigan	Direct Laser Acceleration of Electrons for Bright, Directional Radiation Sources/Relativistic Intensity Laser Channeling and Direct Laser Acceleration of Electrons from an Underdense Plasma
G. Fiksel	University of Michigan	Study of a Self-Generated Magnetic Field in Imploding D^3He Backlighter Capsules and Its Effect on the Properties of the Diagnostic Proton Beams
H. Ji	Princeton University	Thomson-Scattering Measurement of Non-Maxwellian Electrons and Current-Driven Instabilities During Low-Beta Magnetically Driven Reconnection
J. Kim	University of California, San Diego	Efficient Ion Acceleration by Continuous Fields in the Target Transparency Regime
D. Schaeffer	Princeton University (now at University of California, Los Angeles)	Detailed Measurements of Electric and Magnetic Fields in Laser-Driven, Ion-Scale Magnetospheres
D. Schaeffer	Princeton University (now at University of California, Los Angeles)	Particle Heating by High-Mach-Number Collisionless Shocks in Magnetized HED Plasmas
F. H. Séguin	Massachusetts Institute of Technology	Study of Magnetized Plasmas in Shock-Driven Inertial Confinement Fusion Implosions and in Laser-Driven Hohlraums

Measurements of Temperature Evolution in Copper from Intense Proton Beam Energy Deposition

M. Bailly-Grandvaux,[1] C. McGuffey,[2] J. Kim,[1] K. Bhutwala,[1] J. Saret,[1] D. Mariscal,[3] T. Ma,[3] P. M. Nilson,[4] T. Filkins,[4] W. Theobald,[4] A. Haid,[2] S. T. Ivancic,[4] and F. N. Beg[1*]

[1]Center for Energy Research, University of California, San Diego

[2]General Atomics

[3]Lawrence Livermore National Laboratory

[4]Laboratory for Laser Energetics, University of Rochester

[*]Principal Investigator

OMEGA EP can deliver intense proton and ion beams with tens of joules that can then rapidly deposit their energy in bulk samples, leading to isochoric heating of materials into the warm-dense-matter regime. Our group previously studied proton beam transport in thick plastic foams on OMEGA EP, a work that was published recently.[1] Following results from our previous shot day,[2] the FY22 NLUF shot day examined the bulk heating resulting from laser-generated proton beams focused onto solid Cu disks (10- or 25-μm thick $\times$ 200-μm diameter). To quantify the heating, the K_α fluorescence emitted by the Cu was measured with a high-resolution streaked spectrometer (HiResSpec). This diagnostic was used successfully for the first time with proton-heated samples. The Cu temperature was obtained with a few picoseconds resolution and it reached ~50 eV in ~35 ps (Ref. 3).

In the recent FY22 shot day, a steep-walled hollow plastic cone with 100-μm openings at its tip was added where the Cu sample was attached. These cones were used to focus the proton beam into a small spot.[4] The target and diagnostic lines of sight for these shots are shown in Figs. 1(a) and 1(b).

On the primary target configurations discussed above and shown in Figs. 1(a) and 1(b), we collected time-resolved spectra of the K_{α_1} and K_{α_2} and line emissions using the HiResSpec diagnostic in the range of 7.97 to 8.11 keV with a spectral resolution of $E/\Delta E \sim 5000$ and time resolution of ~2 ps. Experimental spectra are compared with spectra calculated using the collisional-radiative spectral analysis code *PrismSPECT*, which together describe the evolution of temperature in the sample and are shown in Fig. 2(a). These spectra are complemented with time-dependent simulations performed with the 1-D radiation-hydrodynamics code *HELIOS*, shown in Fig. 2(b), using as an input the proton beam characteristics inferred from the Thompson parabola ion energy (TPIE) analyzer, radiochromic film diagnostics (RCF), and results from previous work.[4]

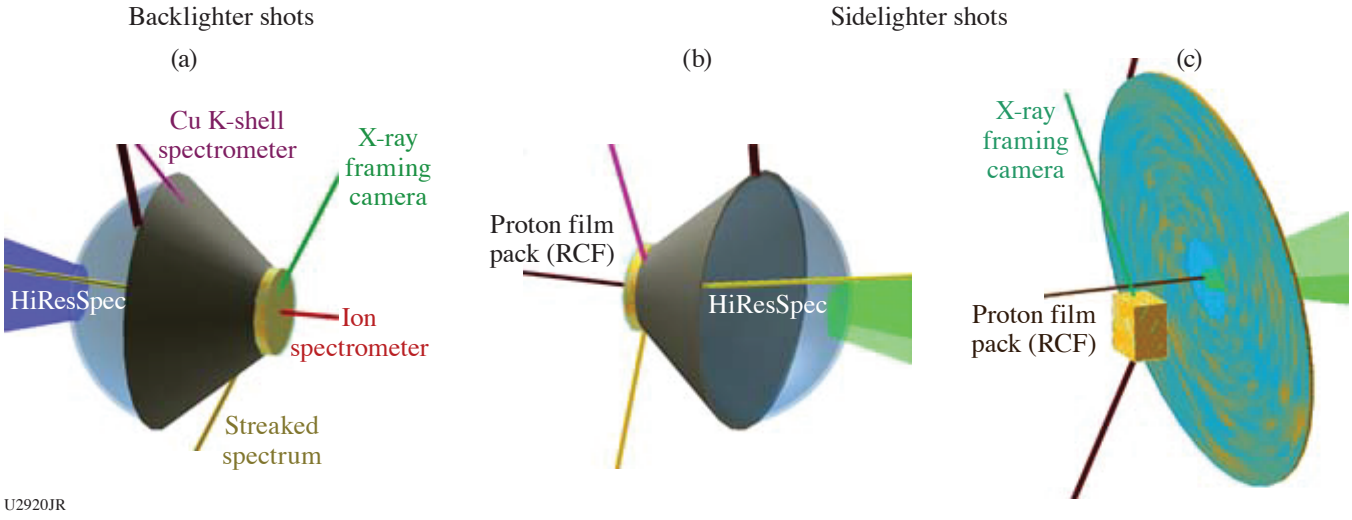

Figure 1
[(a),(b)] Experimental configurations for the Cu disk proton heating experiment. Configurations (a) and (b) used the same laser and target conditions but had complementary diagnostics for the proton beam characterization, an ion spectrometer, or a film pack. Configuration (c) provided a measurement of energy deposition as well as time-resolved images of the top Cu face, giving a cross-sectional view of the emission profile.

The temperature evolution inferred from the *PrismSPECT* analysis and simulated in *HELIOS* are shown in Fig. 2(c). A good agreement was obtained once the sample was heated above 20 eV, into the regime where K_α lines shifts start to be measured.

Remaining analysis includes continued construction of synthetic K_α spectra with more-advanced atomic models to improve comparison with the measured spectra, especially at late times (>50 ps) where the K_α spectra are significantly broadened by spatial gradients and a possible hydrodynamic expansion. Hybrid particle-in-cell simulations using the *LSP* code are also being performed to model the proton and electron transport through the cone and energy deposition into the sample.

We also performed a shot where the proton beam was generated by a thin foil, directed unfocused onto a Cu half block, as shown in Fig. 1(c). Due to the absence of a focusing structure, the measured temperatures were low (<20 eV). With the Cu block intersecting only part of the beam, radiochromic films provided the unblocked and transmitted beam's energy distribution, hence potentially extracting energy deposition. However, significant charging of the Cu block was observed, affecting the measurement.

The experiment was conducted on the OMEGA EP Laser System at the University of Rochester's Laboratory for Laser Energetics with the beam time through the National Laser Users' Facility (NLUF) program. This material is based upon work supported by the Department of Energy, National Nuclear Security Administration under Award Number DE-NA0003943, the University of Rochester, and the New York State Energy Research and Development Authority.

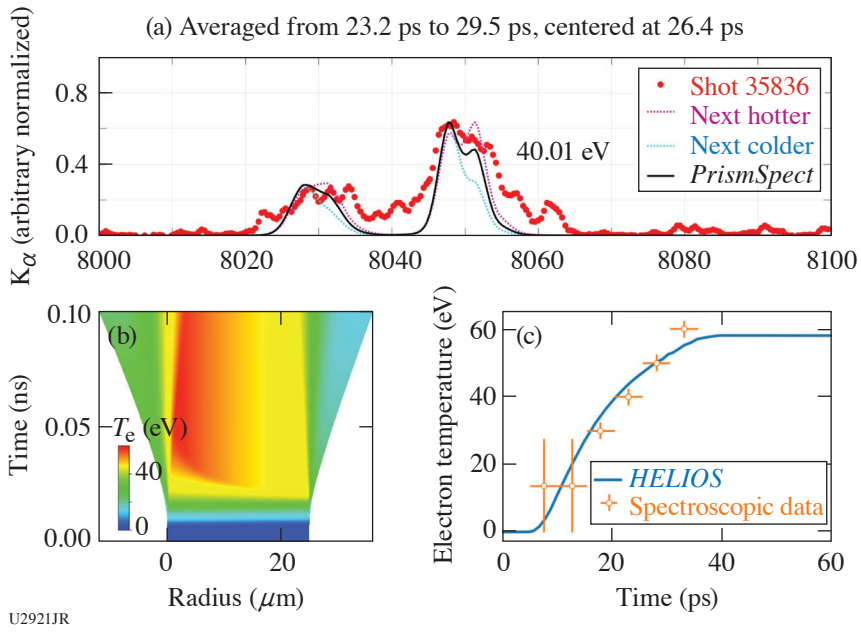

Figure 2
Experimental and simulation results collectively describing temperature evolution in Cu disks. Sample time-integrated spectrum with corresponding iterated time-dependent (a) *PrismSPECT* simulations describe measured temperature evolution and (b) *HELIOS* simulates 1-D temperature evolution. (c) A good agreement in the evolution of sample temperature is obtained once $T > 20$ eV, where K_α line shifts occur.

Magnetic Reconnection in High-Energy-Density Plasmas

W. Fox,[1,2*] D. B. Schaeffer,[2] S. Malko,[1] G. Fiksel,[3] and M. J. Rosenberg[4]
[1]Princeton Plasma Physics Laboratory
[2]Princeton University, Department of Astrophysical Sciences
[3]University of Michigan
[4]Laboratory for Laser Energetics, University of Rochester
[*]Principal Investigator

Magnetic reconnection[5] is a fundamental process in astrophysical plasmas that can convert magnetic energy to plasma kinetic energy, and it underlies processes in cosmic plasmas such as solar flares and substorms in the Eartth's magnetotail. In this project, we conducted laboratory experiments using OMEGA to study how magnetic reconnection proceeds under the conditions of laser-produced plasmas.[5] In these plasmas, magnetic fields are self-generated in the plasma by the Biermann battery effect. Creating two neighboring plumes produces a collision of two magnetized plasmas, driving together the oppositely directed magnetic-field lines and driving magnetic reconnection, which can be observed using the OMEGA suite of plasma diagnostics including x-ray imaging, Thomson scattering, and proton radiography. Laser-produced plasmas are an exciting platform for magnetic reconnection experiments because they can reach a large normalized system size regime, where the plasma is much larger than intrinsic plasma scales such as the electron and ion gyro radius, while simultaneously maintaining low particle collisionality due to high temperature (see Fig. 3). Our recent campaign has conducted experiments at National Ignition Facility and OMEGA, where the range of experiments allows scanning parameters such as the size, temperature, and density of the plasma.[6]

For these particular experiments on OMEGA, we determined that an important and necessary milestone for the project was to improve and validate techniques for analyzing proton radiography data to infer experimental magnetic fields. We therefore devoted several shots to conducting proton radiography measurements of a single expanding plasma plume, which is the simplest possible system to analyze, but which has several pitfalls uncovered in other recent experiments. In particular, our recent work has identified the importance of obtaining and applying boundary conditions on the magnetic field, and second that it is important to deal with intrinsic nonuniformities in the probing proton beam.[6] These new data will allow us to validate techniques for dealing with both issues. Over the rest of the experimental day we obtained additional experimental data on reconnecting plasmas, including Thomson scattering, x-ray images, and proton radiographs. The single-plume experiments, however, are particularly interesting and we present them here in this report.

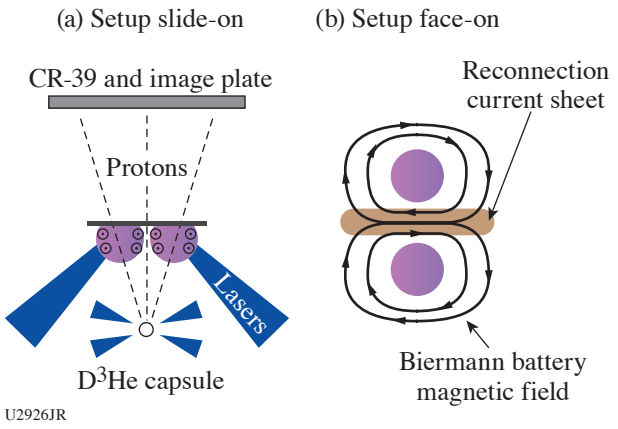

Figure 3
The general setup of laser-driven magnetic reconnection experiments. (a) Side-on view, showing self-generated Biermann-battery magnetic fields in expanding plasmas, and probing of fields by monoenergetic protons from a driven D–^{3}He fusion implosion. (b) Face-on view, showing self-generated Biermann battery fields and formation of a magnetic reconnection current sheet where the two plasmas collide.

For this shot sequence, shown in Fig. 4, we radiographed the evolution of a single plasma plume, driven by two overlapped beams with near-normal incidence, with an on-target energy near 900 J in 1 ns, using standard OMEGA phase plates. The plumes were radiographed after 1.5 ns of evolution, using 15-MeV protons from a imploding D^{3}He capsule. We conducted experiments with three different probing techniques. First, we used a full mesh behind the target [Fig. 4(a)], which breaks the proton beam into multiple beamlets. The magnetic-field strength and direction can be directly inferred from the deflection of the beamlets, albeit at reduced spatial resolution (one data point per beamlet). In addition to the proton data shown here, we additionally obtained an x-ray shadow of the mesh using an image-plate detector at the back of the proton detector stack.[7] The x-ray mesh image provides a direct location of the "undeflected" location of each beamlet.

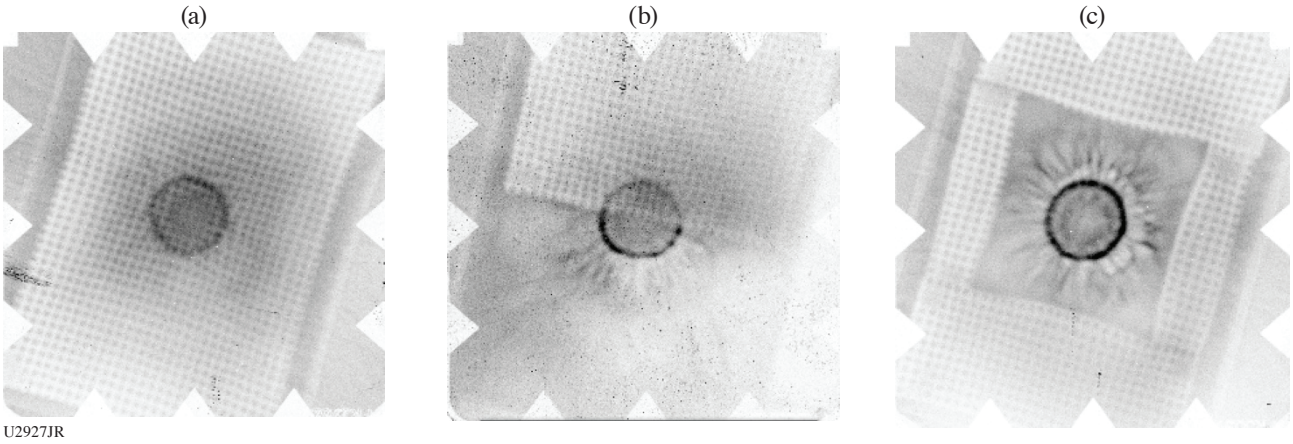

Figure 4
Shown are 15-MeV proton radiographs of expanding plasma plumes. The different experiments show the identical point of evolution of an isolated expanding plume, with three different probing techniques: (a) full mesh behind the foil, (b) half-mesh, and (c) boundary mesh.

We additionally obtained data using a half-mesh [Fig. 4(b)], or boundary mesh [Fig. 4(c)]. In the half-mesh, half of the plume is covered with a mesh, while the other half is a pure-proton-fluence image. In the pure-fluence image, we can observe several features that we commonly see in these plasmas, namely dark circular ring, which is produced by the proton focusing by the global Biermann battery magnetic field wrapping around the plume. Second, we now also observe fine-scale magnetic structures in the plume, which are obscured in the mesh image due to the sacrificed resolution. The pure-fluence data will be analyzed using reconstruction techniques.[6,8] In the half-mesh image, the results can be directly validated against the mesh data, assuming symmetry. Finally, in the boundary mesh case, we will conduct a fluence reconstruction of the central plume, using "help" from outer boundary conditions on the magnetic field, as inferred from the boundary mesh data.

We thank the support of the facility scientists. Experimental time at OMEGA was provided through the LLE Academic and Industrial Basic Science Program. Funding support was provided through Joint FES-NNSA Program in HEDP.

Electron Exhaust Jets and Current-Driven Kinetic Instabilities in Laser-Powered Magnetic Reconnection

S. Zhang,[1] A. Chien,[1] L. Gao,[2] H. Ji,[1,2*] E. G. Blackman,[3] R. K. Follett,[4] D. H. Froula,[4] J. Katz,[4] W. Daughton,[5] C. K. Li,[6] A. Birkel,[6] R. D. Petrasso,[6] J. D. Moody,[7] and H. Chen[7]
[1]Princeton University
[2]Princeton Plasma Physics Laboratory
[3]Department of Physics and Astronomy, University of Rochester
[4]Laboratory for Laser Energetics, University of Rochester
[5]Los Alamos National Laboratory
[6]Massachusetts Institute of Technology
[7]Lawrence Livermore National Laboratory
[*]Principal Investigator

Magnetic reconnection is a ubiquitous phenomenon in space and astrophysical plasmas that rapidly converts magnetic energy into particles and flows. Current-driven instabilities may play an important role in facilitating magnetic energy dissipation. Using two Academic and Industrial Basic Science (AIBS) campaigns on OMEGA, we combined the laser-driven capacitor-coil experiments with time-resolved collective Thomson scattering to study the kinetic physics in the collisionless reconnection, including the evolution of the non-Maxwellian velocity distribution function, electron jets, and kinetic instabilities. Thomson scattering reveals electron-acoustic waves (EAW's) with phase velocities near the electron thermal speed, indicating a non-Maxwellian distribution overcoming Landau damping. We also observed bursty and asymmetric ion-acoustic waves (IAW's), confirming the existence of the electron jet and the current-driven ion-acoustic instabilities (IAI's). The IAW bursts are followed by EAW bursts and electron heating. One- and two-dimensional particle-in-cell (PIC) simulations show that current-driven IAI can form double layers, which induce an electron two-stream instability generating EAW bursts in accordance with the measurements. Our experiments and simulations demonstrate that the electron outflow jet is unstable and can dissipate energy via the nonlinear development of the current-driven instabilities involving electron–ion coupling. We have submitted our findings to Nature Physics and the manuscript is now under review.[9]

The experimental platform is shown in Fig. 5. The capacitor-coil target is made of a 50-μm-thick Cu foil. The coils have a 600-μm diameter and 500-μm-length legs and are separated by 600 μm. The magnetic field generated by the capacitor-coil targets

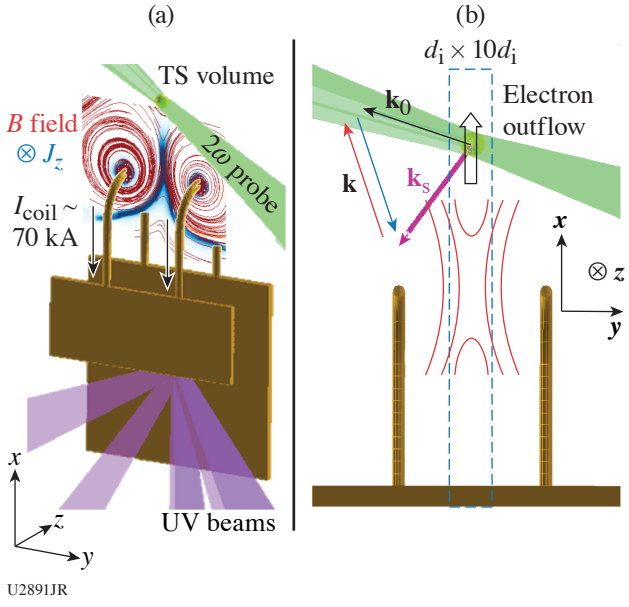

Figure 5
Experimental setup. Six beams of 500-J, 1-ns UV lasers are used to irradiate the back plate of the capacitor, driving current in the coils with $I_{coil} \sim 70$ kA. (a) *FLASH* magnetohydrodynamic (MHD) simulation results are overlapped to show the structure of the magnetic field (red lines) and the out-of-plane current density (blue) in the z direction. A 2ω (527-nm) Thomson-scattering (TS) beam (green) probes the reconnection exhaust region, 600 μm above the center point between the top of the coils. (b) $\mathbf{k}_0$ and $\mathbf{k}_s$ are the wave vectors of the probe beam and the collected scattered light. The red and blue arrows indicate wave vectors ($\mathbf{k}$) of waves in plasma that scatter the probe light to the collector. These $\mathbf{k}$'s are in the x–y plane and 17° off the outflow direction.

is profiled by proton radiography.[10–12] The upstream magnetic field strength is ~40 T at 6 ns after the lasers' onset. The proton radiography also shows the center feature, indicating the reconnection current sheet.

The non-Maxwellian distribution and the kinetic instabilities of the reconnection exhaust are shown in the Thomson-scattering spectrogram . As shown in Fig. 6(a), the IAW-resonant scattering is bursty and asymmetric. The asymmetric IAW spectrum before the bursts can be reproduced in the synthetic TS spectrum with relative drift between electrons and ions as shown in Fig. 6(c). The bursts confirm the existence of the current-driven IAI's. Figure 6(b) shows that the asymmetric IAW peaks are accompanied by an electron-acoustic wave resonant peak, which needs a two-stream distribution as shown in Fig. 6(d) to reproduce.

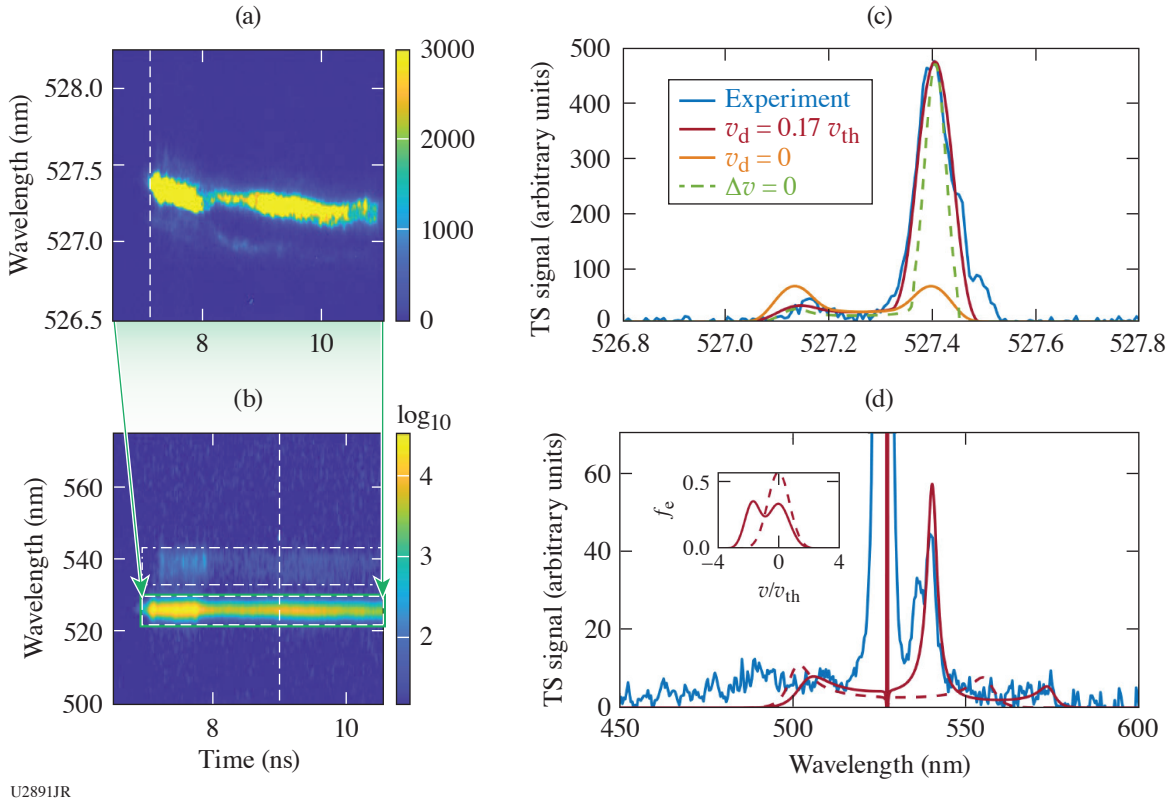

Figure 6
[(a),(b)] Time-resolved Thomson scattering (TS) at $t = 7$ to 10 ns. The IAW resonant peaks in (a) are highly asymmetric (10:1 to 100:1). (c) The spectrum along the vertical dashed line of (a) before the IAW bursts and the comparison with the synthetic TS spectra. The highly asymmetric IAW's can be reproduced with electrons streaming relative to ions with $v_d \sim 0.17\ v_{th}$. (b) The EAW peak along with the IAW feature. (d) The spectrum at 9 ns [along vertical dashed line of (b)] with a fitted synthetic spectrum (red solid line). A two-stream electron distribution is needed to reproduce the strong EAW signal. The distribution is shown as the solid line in the inserted plot. For reference, the synthetic TS spectrum from a Maxwellian distribution is shown as the dashed line.

We acknowledge the Omega Laser Facility staff at the Laboratory for Laser Energetics. This work was performed under the auspices of U.S. DOE NNSA under the AIBS program, and the DOE Office of Science under the HEDLP program with award number DE-SC0020103.

Inertial Confinement Fusion Interface 22A

B. Reichelt and C. K. Li*
Massachusetts Institute of Technology
*Principal Investigator

Inertial Confinement Fusion (ICF) Interface 22A was a makeup shot day for ICF Interface 21A, a separated reactant type shot day from 2021 that had a target assembly issue with out-of-spec glue spots. Like the original experiment, this day aimed to study the issue of interface mix for an 8-μm-thick target using a CD ablator separated from a ^{3}He gas fill by an inert CH layer of varying thickness. Thus, D^{3}He protons and D_2 protons/neutrons provide information about mix since their ratio is proportional to $n_{^3\mathrm{He}}/n_{\mathrm{D}}$. Further, the use of reactions that produce charged particles enables the use of the nuclear-imaging diagnostic proton core imaging spectrometer, which sheds further insight into the region that is producing reactions and how localized the mix is.

This shot day utilized targets that were significantly thinner than previous campaigns in the hopes of probing a regime more dominated by kinetic effects. Of particular interest is determining the accuracy of various mixing models in systems where strong shocks exist, which has become more programmatically relevant as OMEGA cryo shots have worked to increase implosion velocity. Both hydrodynamic and fully kinetic models are being interrogated using the LANL codes *xRAGE* and *iFP*, respectively.

Early analysis of nuclear data has been done to determine the charged-particle spectra emitted from the implosion shown in Fig. 7. As shown, the relationship between the CH buffer layer thickness and the spectral peak/width is not immediately apparent, but might be possible to relate to implosion ρR through stopping power and straggling formulas. There are interesting trends seen in the yields, however, which show an inversion effect as a function of offset thickness similar to past experiments for thicker capsules with lower temperatures.[13] Work is ongoing to analyze the time and spatially resolved nuclear diagnostic data collected by this experiment and to compare to predictions from hydrodynamic and kinetic simulations.

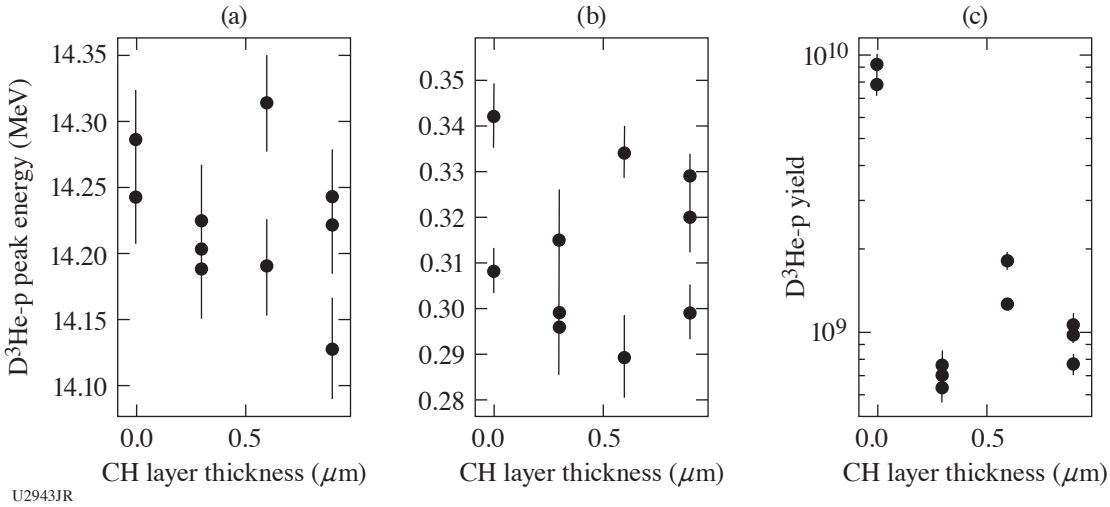

Figure 7
Analysis of D^{3}He proton spectra data from ICF Interface 22A using the wedge-range-filter array diagnostic.

This work is funded by DOE/NNSA Center of Excellence Contract DE-NA0003868. B. Reichelt is supported by NNSA Stewardship Science Graduate Fellowship Contract DE-NA0003960.

Effects of an External Magnetic Field on Laser–Plasma Instabilities

M. Bailly-Grandvaux,[1*] S. Bolaños,[1] R. Lee,[2] M. J.-E Manuel,[3] W. B. Mori,[2] F. Tsung,[2] B. Winjum,[4] and F. N. Beg[1]
[1]Center for Energy Research, University of California, San Diego
[2]Physics and Astronomy Department, University of California, Los Angeles
[3]General Atomics
[4]Office of Advanced Research Computing, University of California, Los Angeles
[*]Principal Investigator

Laser–plasma instabilities (LPI's) play a detrimental role in energy coupling to the target in inertial confinement fusion (ICF). This fundamental constraint of energy coupling of high-power lasers to plasma has been studied extensively over the last couple of decades under a wide variety of laser and plasma parameters. The recent development of applied strong magnetic fields for use in ICF and laboratory astrophysics experiments, however, has opened opportunities to investigate the role of external magnetic fields on LPI's. Recent numerical studies have shown that stimulated Raman scattering (SRS)[14] can be mitigated by external magnetic fields in the kinetic regime of the instability and warrant systematic experimental studies to validate modeling.

With this aim, we developed a platform for OMEGA EP to investigate the effect of an external magnetic field on SRS. A first shot day experiment was carried out in FY20, where we successfully demonstrated the feasibility to investigate backward-SRS (BSRS) in the kinetic regime and in a magnetized environment.[15] The experiment relied on the ability to measure the BSRS light when a laser pulse propagated through a magnetized gas-jet target, as sketched in Fig. 8(a). To measure the backscattered light, we used the sub-aperture backscatter (SABS) diagnostic, which provided a temporal and spectral resolution. The dual magneto-inertial fusion electrical discharge system (MIFEDS) ten-inch manipulator (TIM)-based pulsed-power device was fielded to embed the gas jet in a quasi-perpendicular and uniform magnetic field of ~22 T. The Rowland x-ray spectrometer and the 4ω-probe diagnostics suite were fielded in order to estimate the plasma conditions by comparing them with radiation-magnetohydrodynamic simulations (using *FLASH* and *GORGON* codes). We modified the platform in light of the first shot day experience: the MIFEDS axis was oriented in the same direction as the gas flow [Fig. 8(a)]. We also modified the laser profile of the interaction beam [orange curve in Fig. 8(b)] and added a heater beam. The main benefit of the heater beam is to prepare the plasma prior to the excitation beam interaction with improved uniformity. Its larger size reduces gradients within the smaller excitation beam spot size and lowers the intensity on target to avoid filamentation during heating. The SRS driver (Beam 4) utilized a special laser shape (a train of short pulses) to aid the interpretation of the BSRS signal by drastically reducing temporal variations of plasma conditions within the interaction of a 100-ps pulse.

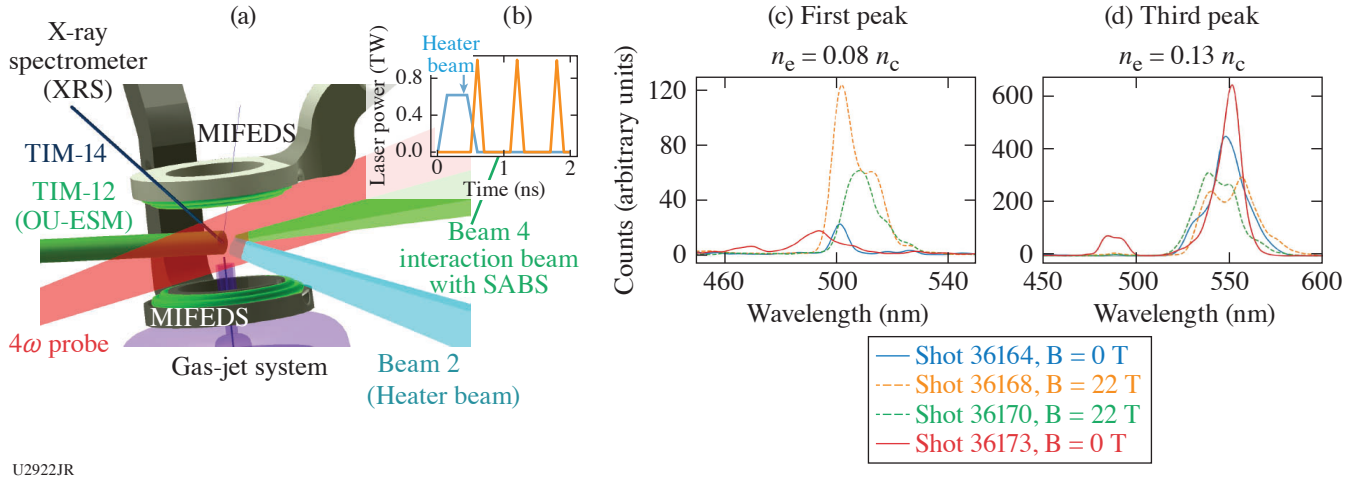

Figure 8
(a) *VISRAD* schematic of the experimental platform. (b) Temporal profiles of the laser power at target chamber center. [(c),(d)] Spectra of the backscattered light measured with SABS. Solid lines are shots without an external B field, and dashed lines are shots with an applied B field of 22 T. Spectra of the (c) first peak (d) the third peak. Note that the density is estimated according to the wavelength shift. OU-ESM: Osaka University electron spectrometer.

In the latest MagSRS-22A campaign, seven shots were performed. The first two shots of the day were performed with an argon pressure of 550 psi. The following shots were performed with a pressure of 880 psi in order to reach a higher density and thus reach the desired kinetic regime ($k\lambda_D \sim 0.2$ to 0.35). Three out of the five 880-psi shots were magnetized shots. We note that in one magnetized shot, MIFEDS failed, likely due to an arcing effect.

The SRS emission excited by a train of short 100-ps pulses is separated in the streaked spectral measurements, making it possible to correlate the spectra to specific plasma conditions for each pulse, as illustrated in Figs. 8(c) and 8(d). Since the time between pulses (~600 ps) is larger than the hydrodynamic time scale, the SRS excitation occurs in different conditions, meaning we diagnose the magnetic effect in various regimes. Figures 8(c) and 8(d) show the spectra measured with the SABS diagnostic for the first and third pulses where we observe contradictory behavior in the presence of the applied B field. For the third peak [$n_e \sim 13\%\ n_c$, see Fig. 8(d)], we observe mitigation of SRS reflectivity in the presence of the external B field, as expected. This is the first experimental evidence of SRS mitigation with B field. On the other hand, for the first peak [$n_e \sim 8\%\ n_c$, see Fig. 8(c)], we observe an apparent enhancement of the SRS reflectivity when applying an external magnetic field. We suspect that this enhancement is due to a rescattering mechanism. For the second peak (not shown) the backscattered light spectra are shifted to a wavelength corresponding to lower densities of $n_e \sim 5\%\ n_c$, although the data were not reproducible for repeated shots. As seen by the shift of the BSRS wavelength, shot-to-shot variations are related to hydrodynamic fluctuations that seem to be significant ~1 ns after the laser–plasma interaction (heater beam) and averaged out later in time.

We estimate the electron density from the backscatter wavelength. Indeed, the backscatter wavelength is strongly dependent on electron density. The electron temperature also induces a small shift. We fielded the Rowland x-ray spectrometer to estimate an average temperature of ~800 eV. Figure 9(a) shows the time-integrated K-shell emissions from the Ar gas jet and the synthetic spectra calculated by the collisional-radiative spectral analysis code *PrismSPECT*. With this measurement, we were able to correct the estimation of the electron density from the wavelength shifts in the backscatter spectra.

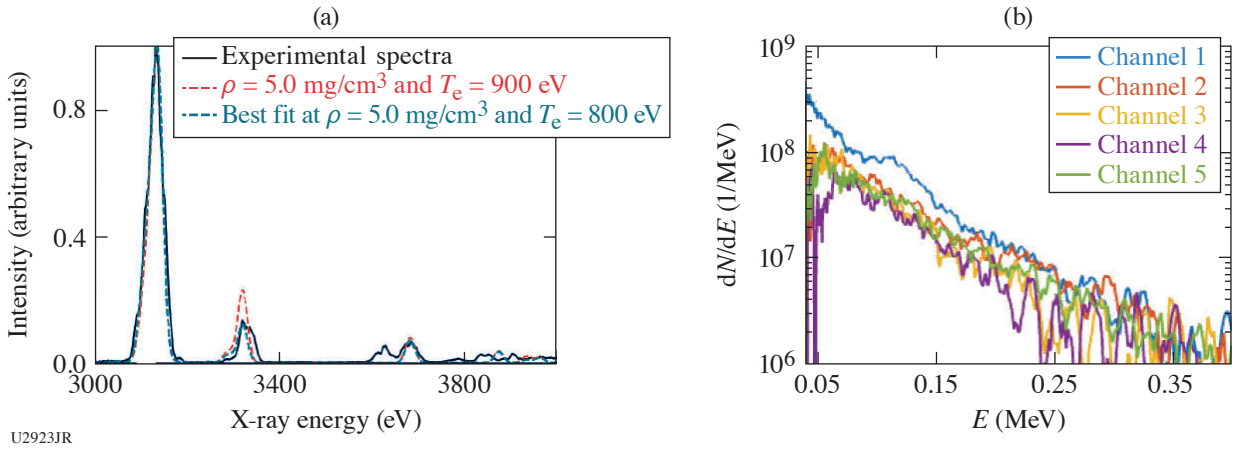

Figure 9
(a) XRS signal with a fit using *PrismSPECT*, giving an average electron temperature of ~800 eV. (b) Electron spectra measured at various angles via the OU-ESM.

In the studied regime, the wave-particle interaction plays a crucial role. A part of the electrons become trapped in the electron plasma wave and are accelerated at the phase velocity of the electron plasma wave in the direction of the laser. We fielded the OU-ESM electron spectrometer to measure the energy distribution of hot electrons. When unmagnetized, these hot electrons reduce the Landau damping and enable the growth of the SRS at $k\lambda_D \sim 0.3$. Figure 9 shows the electron spectra measured on one of the unmagnetized shots with a pressure of 880 psi. It reveals the presence of hot electrons with a temperature reaching ~300 keV, while no electrons were detected at the lower pressure of 550 psi. The OU-ESM is angularly resolved, such that each of the channels collects a sample of the electron beam at a different angle. Here, channel 1 is the channel the most aligned with the SRS driver

beam (Beam 4). We note an increase in the number of electrons (×2) for $E < 150$ keV, suggesting they were probably accelerated by the electron plasma wave induced by the SRS driver. Yet, the measured temperature is above our expectation and suggests that other LPI's occurred.[16] More particle-in-cell simulations will be run to understand the origin of such hot electrons. We did not detect any electrons in magnetized shots due to the deflections by the large-volume B field generated by the MIFEDS coils.

The experiment was conducted on the OMEGAG EP Laser System at the University of Rochester's Laboratory for Laser Energetics with the beam time through the NLUF Program. This material is based upon work supported by the Department of Energy, National Nuclear Security Administration under Award Numbers DE-NA0003842 and DE-NA0003856, the University of Rochester, and the New York State Energy Research and Development Authority.

Pressure Induced B1–B2 Phase Transition in ZnO Under Laser-Driven Ramp Compression

I. K. Ocampo,[1] D. Kim,[1] F. Coppari,[2] R. F. Smith,[2] and T. S. Duffy[1*]
[1]Department of Geosciences, Princeton University
[2]Lawrence Livermore National Laboratory
[*]Principal Investigator

ZnO is a wide-band-gap semiconductor (3.37 eV) well suited for use in electronic and optoelectronic devices (UV emission lasers and detectors, chemical sensors, and solar cells).[17] At ambient conditions, ZnO crystallizes in the wurtzite-type structure (B4, $P6_3mc$). Under quasi-hydrostatic loading, ZnO undergoes a phase transition from a B4-type to a B1-type structure (*Fm-3m*) at ~10 GPa (Ref. 18). Although no further phase transitions have been observed in ZnO experimentally up to ~209 GPa, density functional theory calculations predict that the B2 phase (*Pm-3m*) will become stable at high pressures. The calculated B1–B2 transition pressure varies by approximately 25% between two existing computational studies.[19,20] A tetragonal phase (B10, *P4/nmm*) has also been predicated to become thermodynamically stable over a narrow pressure region (236 to 316 GPa). In this study, we utilized the pulse-shaping capabilities of the OMEGA laser to ramp compress ZnO up to ~800 GPa and probe the atomic level structure of highly compressed ZnO using the powder x-ray diffraction image-plate (PXRDIP) diagnostic. These experiments allow us to directly test theoretical predictions of phase stability and equations of state.

Polycrystalline ZnO foils were synthesized by cold-pressing ZnO powders at 1.7 GPa in a diamond-anvil cell with 800-μm culets. Scanning electron microscope images of the foils were used to estimate the porosity of the foils (~3%). The ZnO foils were sandwiched between an ablator and a single-crystal diamond (SCD) tamper. The ablator for these experiments consisted of two SCD plates with a thin gold coating deposited in between, which acts to shield heat generated at the ablation surface. The ablator–ZnO–tamper target package was then centered over a Ta foil with a 300-μm pinhole and mounted onto the front of the PXRDIP diagnostic box. A 7- to 10-ns ramp shaped pulse was used to ablate the surface of the target package and quasi-isentropically compress the sample. When the target was expected to be at peak stress according to pre-shot hydrocode simulations, a 1-ns laser pulse was used to irradiate a Cu backlighter foil, generating quasi-monochromatic x rays (8.37 keV) that were diffracted from the target and recorded using the PXRDIP diagnostic. A line-VISAR (velocity interferometer system for any reflector) was used to monitor the planarity of the laser drive as well as the particle velocity at the SCD tamper-free surface. We used a Monte Carlo backward-propagating characteristics algorithm to infer the stress history in the sample and estimate the uncertainty in the achieved stress during the x-ray flash.

We have previously reported a series of laser-driven, ramp-compression experiments on ZnO with peak stresses from 260 to 620 GPa where we observed the onset of the B1–B2 phase transition between 299 and 332 GPa. This result is in very good agreement with theoretical predictions. Preliminary analyses of these data also suggest that the B1 and B2 phases remain in coexistence from 330 to 620 GPa. This shows that ramp compression can produce a remarkably large mixed-phase region. In our recent campaign, XRDEOS-22A-NLUF, we conducted four new experiments on OMEGA, extending the pressure–density data for this material up to 800 GPa. At 650 GPa, only the B2 phase was observed. To test the repeatability of this result, another experiment was conducted at 651 GPa and again, only the B2 phase was observed. This provides a high accuracy constraint on the extent of the B1–B2 mixed-phase region under ramp compression (300 to 650 GPa). The extreme metastability of the B1-type structure under the nanosecond time scales of our experiments suggests a kinetic limitation to the B1–B2 transition, yet further experi-

ments are required to evaluate the role of non-hydrostaticity and material strength on this fundamental phase transformation. The diffraction results from our experiment at 800 GPa are shown in Fig. 10. Two sample diffraction peaks could be indexed as corresponding to the (010) and (011) reflections of the B2-type structure. At this stress, ZnO has experienced a more than 2.6-fold increase in its ambient density. This work is ongoing and further experiments will be conducted to develop a pressure–density equation of state of the high-pressure B2 phase.

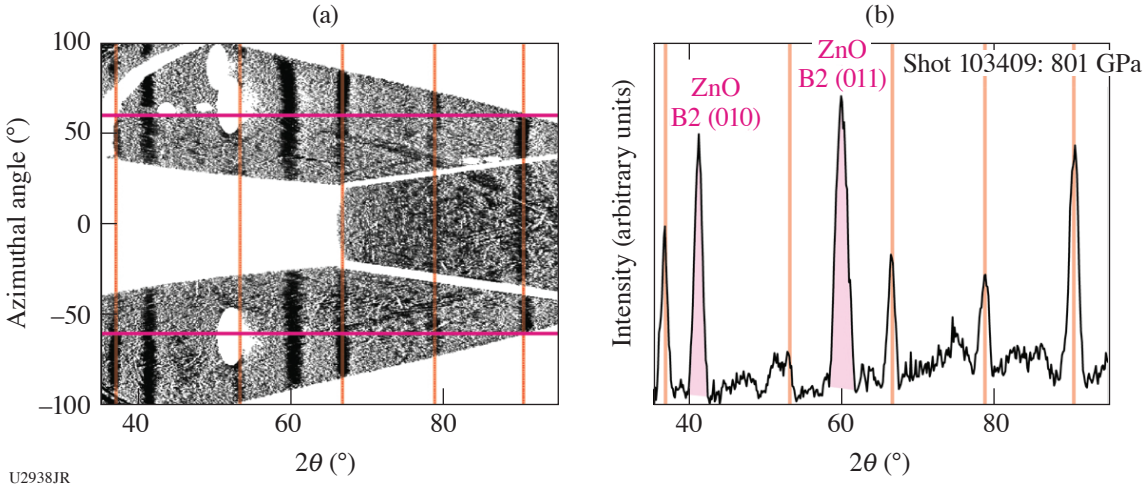

Figure 10
Diffraction results from shot 103409, our highest stress experiments (801 GPa). (a) The dewarped image plates projected into 2θ–ϕ space. Orange vertical lines highlight diffraction from the Ta pinhole. (b) The 1-D diffraction pattern integrated over the azimuthal angles specified by the horizontal magenta lines.

This work was supported by DOE Office of Science, Fusion Energy Sciences under Contract No. DE-SC0020005, the LaserNetUS initiative at the Omega Laser Facility, NNSA Contract No. DE-NA0003957, and National Science Foundation (NSF) EAR-1644614.

MultiIon Campaign: Studies of Multi-Ion and Kinetic Effects in Shock and Ablatively Driven Implosions

T. Evans,[1] N. V. Kabadi,[2] P. Adrian,[1] J. Kunimune,[1] E. Gallardo-Diaz,[3] R. C. Mancini,[3] C. Stoeckl,[2] V. N. Glebov,[2] and J. A. Frenje[1*]
[1]Plasma Science and Fusion Center, Massachusetts Institute of Technology
[2]Laboratory for Laser Energetics, University of Rochester
[3]University of Nevada, Reno
*Principal Investigator

MultiIon-22A and MultiIon-22B focused on studying the impact of multi-ion and kinetic effects on several observables during the shock-burn phase and subsequent compression phase in both shock- and ablatively driven implosions. Previous work demonstrated the presence of thermal decoupling and a significant deviation from hydrodynamic behavior of implosions with low initial gas-fill density (or pressure).[21,22] Yield, ion temperature, emission histories of x rays, neutrons, and protons were measured simultaneously in each implosion experiment. The measured data set is being compared to both hydrodynamic and kinetic simulations to understand the influence of multi-ion and kinetic effects at different stages of an ICF implosion.

As shown in Fig. 11, the MultiIon-22A experiment featured 2.8-μm Hoppe-glass capsules with four different initial gas-fill densities, ranging from 0.5 mg/cm^3 to 3.5 mg/cm^3. The variation in initial gas-fill density was selected to obtain a range of Knudsen numbers (K_n) spanning the transition from kinetic to hydro-like behavior. K_n is defined as the ratio of the ion–ion mean free path to the system size (radius of the shell), and is proportional to the square of the temperature over density:

$$K_n = \frac{\lambda_{ii}}{R_{\text{shell}}} \propto \frac{T^2}{n}.$$

Data demonstrate a large discrepancy between the yield in the lower-density cases and that predicted by hydrodynamic theory alone, even where hydrodynamic simulations effectively match other key implosion parameters, including bang time and ion temperature (see Fig. 12). Further analysis of data from this shot day will include comparison to fully kinetic simulations, which are expected to recreate the observed discrepancy.

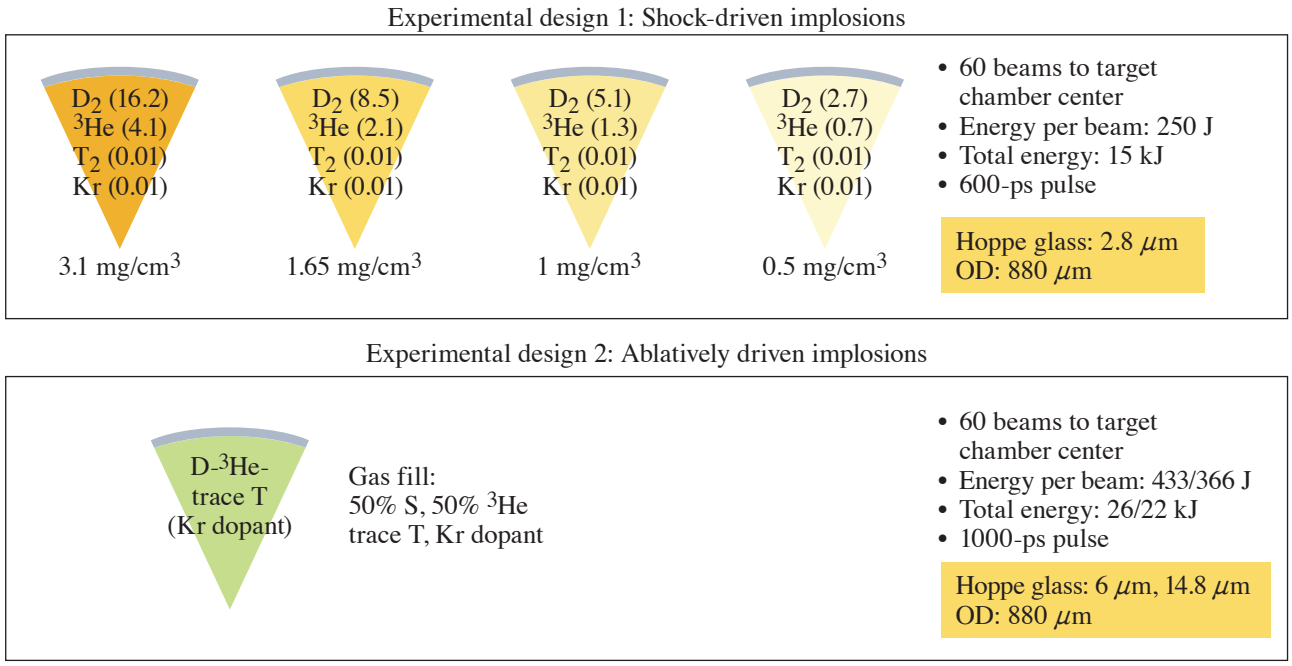

Figure 11
Capsule and laser specifications for both MultiIon-22A and MultiIon-22B experiments.

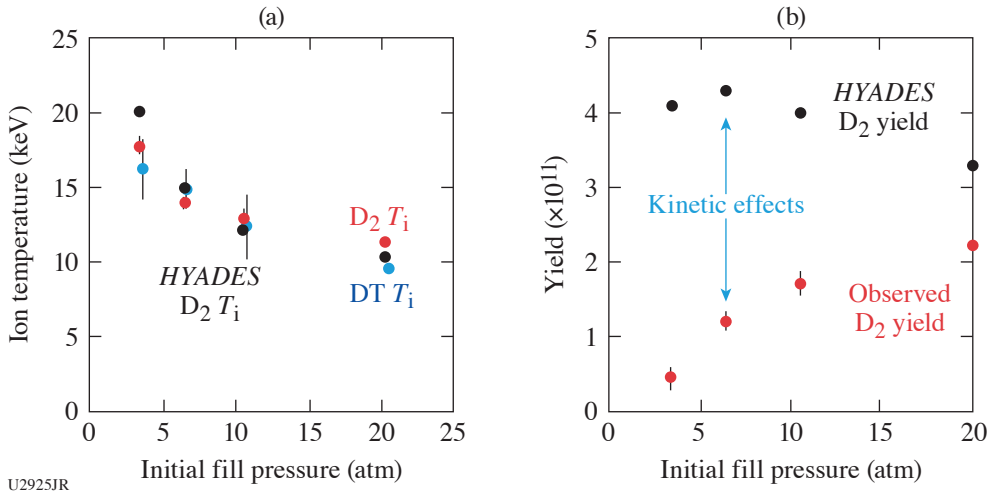

Figure 12
(a) Measured and hydro-simulated D_2 and DT ion temperature versus initial gas-fill pressure. A preliminary evaluation suggests a good agreement between data and simulation is observed. (b) Measured and hydro-simulated D_2 yield versus initial gas-fill pressure. The yield shows a large discrepancy at lower fill pressures, clearly indicating the impact kinetic effects, which will be further analyzed.

The MultiIon-22B experiment featured 6-μm and 15-μm-thick Hoppe-glass capsules that were illuminated by two different laser driver energies. The purpose with these capsule and laser configurations was to generate compression-driven implosions and study how kinetic effects persist from the shock-burn phase to the subsequent compression phase. In addition, the different shell thicknesses and laser energies provide different shock strengths. The analysis of the resulting data is ongoing and will involve both hydrodynamic and kinetic simulations with the intention of linking key implosion parameters to those observed in MultiIon-22A.

In summary, excellent data were obtained with the primary particle x-ray temporal diagnostic[23] and neutron temporal diagnostic in both the MultiIon-22A and MultiIon-22B experiments. The analysis of the resulting data is underway. Continued analysis will link the results of the two shot days and inform a dynamic model of the impact of shock-burn phase kinetic effects on the subsequent compression phase.

This work was supported by DOE/NNSA contracts DE-NA0003868, DE-NA0003856, and DE-NA0003938. Thank you to collaborators at MIT and LLE for support and guidance.

Ablator–Gas Interface Dynamics and Mix in Inertial Confinement Fusion-Relevant Conditions

J. Kunimune,[1] B. Reichelt,[1] P. Adrian,[1] S. Anderson,[2] B. Appelbe,[3] A. Crilly,[3] T. Evans,[1] C. J. Forrest,[4] J. A. Frenje,[1] V. Yu. Glebov,[4] B. M. Haines,[2] T. M. Johnson,[1] C. K. Li,[1] H. G. Rinderknecht,[4] G. D. Sutcliffe,[1] W. Taitano,[2] and M. Gatu Johnson[1*]
[1]Massachusetts Institute of Technology
[2]Los Alamos National Laboratory
[3]Imperial College, London
[4]Laboratory for Laser Energetics, University of Rochester
[*]Principal Investigator

The main goal of this NLUF campaign is to validate and confirm the impact of "kinetic mix,"[24] where fast streaming ions generated during the shock phase of an ICF implosion impact core plasma conditions. Reaching this goal also requires quantifying the relative impact of other mix effects (hydro-instabilities, diffusion, and localized mix) as a function of implosion conditions (to isolate the kinetic mix effect, these other effects must be mitigated or understood). During FY22, two initial experiments were executed as part of this project: LocMix-22A (0.5 shot days, PI MIT Ph.D. student Justin Kunimune) and KinMix-22A (one shot day, PI MIT Ph.D. student B. Reichelt).

Targets for LocMix-22A and KinMix-22A are shown in Fig. 13. All were filled to the same number density and had the same outer diameter, and both campaigns used both 6-μm and 15-μm-thick plastic shells to vary implosion conditions from more kinetic (6 μm) to more hydro-like (15 μm), with the anticipation that kinetic and diffusion mix will dominate at 6 μm with hydro (instability) mix starting to play more of a role at 15 μm.

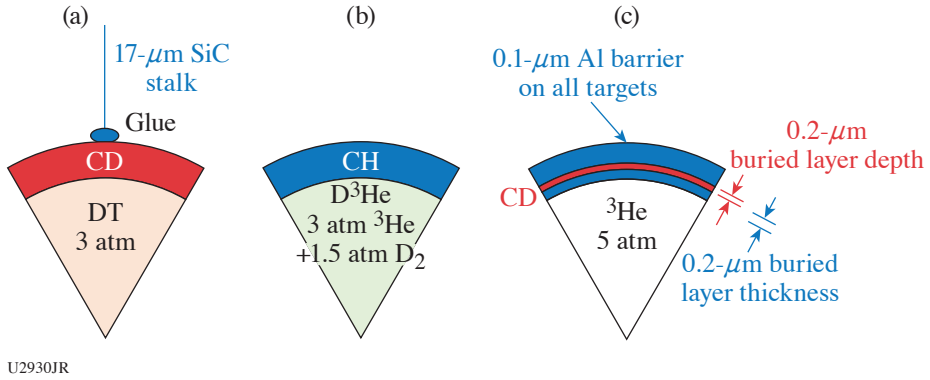

Figure 13
Pie diagrams for targets used for (a) LocMix-22A and [(b),(c)] KinMix-22A. For each experiment, total shell thickness of 6 μm and 15 μm were used to vary implosion conditions from strongly shock driven and thus highly kinetic (6-μm shell) to more compressively driven and hence more hydro-like (15-μm shell). The goal of LocMix-22A was to quantify localized mix due to stalk impact by using imaging diagnostics and one to two stalks, while the goal of KinMix-22A was to study the balance of diffusion/kinetic/hydro mix as a function of implosion conditions using nuclear observables with time-resolved nuclear burn-history measurements as the primary diagnostic.

The specific goal of LocMix-22A was to measure impact of localized mix due to the capsule stalk mount. To this end, half of the implosions used a single stalk, while half used two stalks in opposing geometry. The primary diagnostics were three-axis x-ray and knock-on deuteron (KOd) imaging (Fig. 14). Three x-ray images in different energy bands were obtained in each of three near-orthogonal viewing directions; these data will be used to reconstruct spatial electron temperature profiles. *xRAGE* simulations predict that the effect of the stalk mix will be a region of less x-ray emission due to injection of material that is ~2 keV colder than the surrounding fuel;[25] if correct, this should be clearly visible in the x-ray data. The KOd come from DT neutrons scattering off of D in the fuel or CD shell. By imaging deuterons in different energy bands, differences in morphology of the fuel (high-energy, forward-scattered deuterons) and shell (lower-energy, side-scattered deuterons) should be discernible. Analysis of both x-ray and KOd images are still in the early stages; preliminary images from the TIM-4 viewing angle are also shown in Fig. 14.

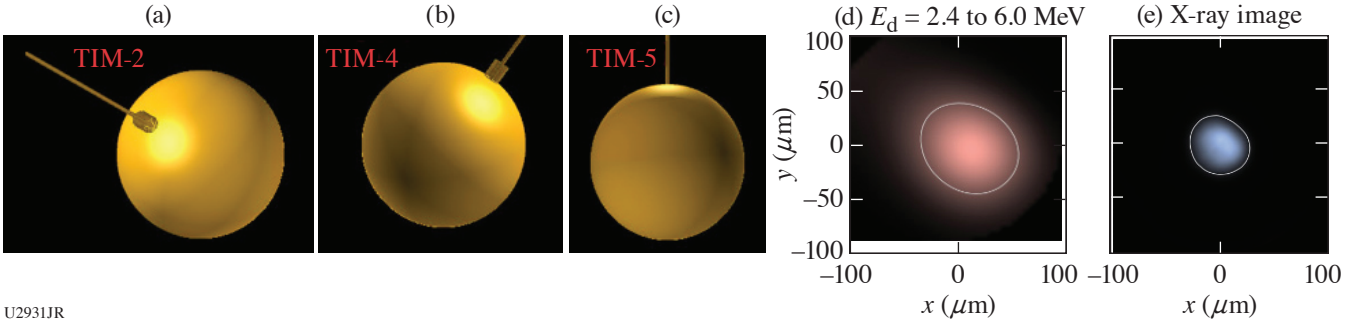

Figure 14
[(a)–(c)] LocMix-22A used three near-orthogonal penumbral imaging detectors in OMEGA TIM-2, -4, and -5 set up to measure (d) knock-on deuterons and (e) x rays in three different energy bands. (d) The TIM-4 deuteron image in the 2.4- to 6.0-MeV energy band, and (e) the x-ray image recorded in the same location. Analysis is in progress to infer stalk impact through reconstruction of the spatial electron temperature distribution from the x-ray images in different energy bands, and through the study of asymmetries in the knock-on deuteron emission.

KinMix-22A used directly comparable buried-layer targets, with a CD tracer layer and pure ^{3}He gas fill, and reference targets, with CH shells and 50:50 D^{3}He fill, to study the level (through integrated nuclear signatures) and timing (through nuclear burn history measurements) of mix. Detailed analysis of the data is in progress; preliminary D^{3}He yields show substantially more mixing for the thin shell (6 μm) than thick shell (15 μm) targets (Table II). The particle x-ray temporal diagnostic (PXTD) also recorded good data on this experiment, which will be used to address the relative timing of proton emission versus peak convergence for the two shell thicknesses, thus helping constrain the mix mechanisms responsible for injecting deuterium into the fuel as a function of implosion conditions.

Table II: Highly preliminary results from KinMix-22A suggest substantially more shell mixing (D^{3}He signal) for the 6-μm shells than for the 15-μm shells (10% of the control versus 2% of the control D^{3}He yield, respectively). CR-39 etching and scanning is still in progress to finalize these numbers. nTOF: neutron time of flight.

Total shell thickness (μm)	Capsule fill	Laser pulse	YDD$_n$ estimated (nTOF)	YD^{3}He$_P$ estimated (nTOF)	DD$_n$ temperature (nTOF)
14.3	4.5 atm D^{3}He	SG010	1×10^{10}	6×10^9	6 keV
14.6	5 atm ^{3}He	SG010	2.5×10^8	1×10^8	2.5 keV
6.3	5 atm ^{3}He	SG006	4×10^7	1×10^9	Uncertain (5 to 15 keV)
5.8	4.5 atm D^{3}He	SG006	1.5×10^{10}	1×10^{10}	15 keV

The KinMix-22A and LocMix-22A datasets will be completed with further buried-layer data from KinMix-23A, and with measurements of the ion release from 6-μm and 15-μm flat foils in opposing geometry with a gas jet in between, using Thomson scattering and x-ray imaging, on FoilGasDist-23A.

This material is based upon work supported by the National Nuclear Security Administration, Stewardship Science Academic Alliances, under Award Number DE-NA0003868. The experiments were conducted at the Omega Laser Facility with the beam time through the NLUF under the auspices of the U.S. DOE/NNSA by the University of Rochester's Laboratory for Laser Energetics under Contract DE-NA0003856. B. Reichelt is supported by NNSA SSGF Contract DE-NA0003960.

Report for DACPlanet-22A/B

G. Tabak,[1,2*] G. W. Collins,[1,2,3] J. R. Rygg,[1,2,3] R. Dias,[2,3] N. Dasenbrock-Gammon,[2] T.-A. Suer,[1,3] S. Brygoo,[4] P. Loubeyre,[4] and R. Jeanloz[5*]
[1]Laboratory for Laser Energetics, University of Rochester
[2]Department of Physics and Astronomy, University of Rochester
[3]Department of Mechanical Engineering, University of Rochester
[4]Commissariat à l'énergie atomique et aux energies alternatives
[5]University of California, Berkeley
[*]Principal Investigators

The purpose of this campaign was to study a hydrogen–neon gas mixture with planetary science applications in mind. Hydrogen and neon are present in gas giants such as Saturn and the two are predicted to be immiscible at certain pressure–temperature conditions inside these planets. Documenting the exact location of the demixing boundary has implications for planetary modeling. This study is a follow-up on similar experiments performed on hydrogen–helium mixtures.[26]

The experimental approach was to precompress H_2–Ne mixtures (20% Ne by mole) in diamond-anvil cells (DAC's) to 4 GPa and shock compress them using the high-power lasers at LLE. At the 4-GPa precompression, hydrogen and neon are liquid and miscible, making it possible to prepare a homogeneous sample at liquid initial densities. The resulting Hugoniot curve is predicted to span pressure–temperature conditions relevant to planets and cross the demixing boundary, beyond which (i.e., at the most extreme conditions) the hydrogen and neon are miscible. A quartz layer was inserted into the DAC chamber to serve as a material standard. The filled DAC's were characterized to measure the sample pressure and chamber thickness. The targets were then driven with a 1-ns square pulse drive on the OMEGA 60-beam laser, driving a shock wave through the samples. VISAR and SOP (streaked optical pyrometry) were used to measure the shock velocity, reflectivity, and self-emission.

Excellent velocimetry and pyrometry data were obtained using VISAR and SOP (see Fig. 15). Impedance matching with quartz will be used to infer the pressure and density of the gas mixture. The self-emission and VISAR fringe amplitude will be referenced to quartz to measure the reflectivity and temperature of the shocked gas mixture. The expected signature of the demixing boundary is a discontinuity in the reflectivity along the Hugoniot. Such a signature has been observed for hydrogen–helium mixtures.[26]

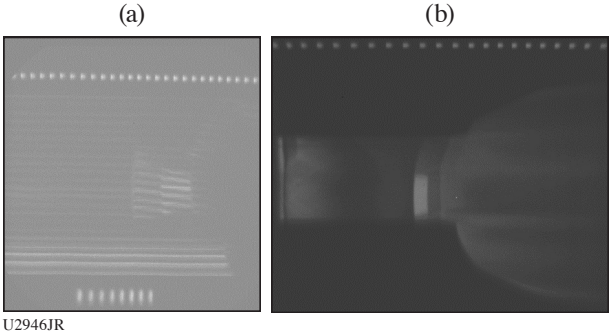

Figure 15
(a) VISAR and (b) SOP data for shot 103818. The two fringe events at the spatial center of the streak camera image indicate shock breakout into quartz and then into the gas mixture. The self-emission of the quartz standard is clearly seen as the small rectangular region on the SOP image, after which the gas mixture self-emission is recorded.

Several data points on the hydrogen–neon mixture have been obtained, providing the first step to understanding the mixture. Additional data will be obtained in FY23 that should provide definitive evidence of the expected reflectivity discontinuity in order to demarcate the demixing threshold. In particular, more shots at lower pressures (<150 GPa) are needed to study the region of interest. The resulting impedance match with quartz would entail a quartz sample that is either absorbing or transparent at the

VISAR probe frequency (532 nm), so some targets will be prepared instead with a fused-silica window. The fused silica becomes reflective at lower pressures than quartz, so this will facilitate lower shock pressure experiments with a reflective material standard.

Plasmoid Magnetic Reconnection Between Long-Pulse, Laser-Driven Plasmas Perturbed by a Short-Pulse Laser

J. L. Latham,[1] B. K. Russell,[1] L. Willingale,[1] P. T. Campbell,[1] G. Fiksel,[1] P. M. Nilson,[2] and K. M. Krushelnick[1*]
[1]Center for Ultrafast Optical Science, University of Michigan
[2]Laboratory for Laser Energetics, University of Rochester
[*]Principal Investigator

To understand magnetic reconnection in high-energy-density plasmas,[27] this campaign studied the magnetic fields of a three-pulse geometry, where a short-pulse laser illuminated the interaction region between two expanding plasma plumes, each driven by a long-pulse laser. Pre-shot studies anticipated that the reconnection rate would increase with the temperature of the interaction region, à la plasmoid reconnection theory,[28] but that the outflowing plasma from the short-pulse laser would inhibit reconnection.

In the experiment, plastic targets were irradiated by two UV beams with an intensity of 1.1×10^{14} W/cm^2 for 2.5 ns ("long-pulse lasers"). Some of the targets were also irradiated by an IR beam with an intensity of 2×10^{19} W/cm^2 for 10 ps ("short-pulse laser"). The resulting magnetic (and electric) fields were recorded in radiochromic film (RCF), using a proton beam created by a second short-pulse laser incident at a copper foil located 8 mm away from the target. The data show dark rings around each of the laser spots, and in several cases a highly complicated structure (Fig. 16).

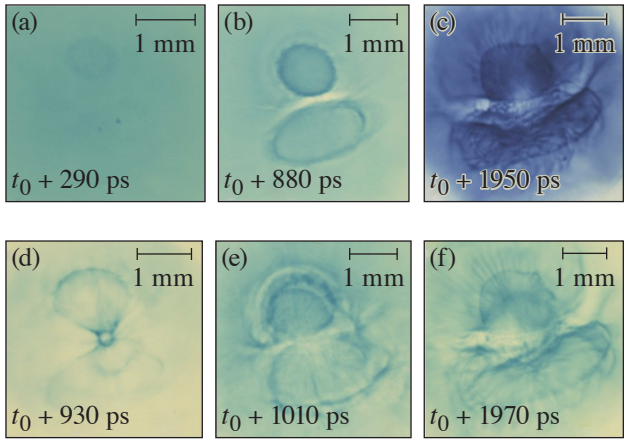

Figure 16
Scans of RCF irradiated by 24-MeV protons that passed through the main laser target. The time that the proton beam passed through the target is indicated on each film where t_0 is the onset of the UV beams. For shots (a)–(c) there was no short-pulse laser on the main target. For films (d)–(f), the short-pulse laser arrived at times t_0 + 360 ps, t_0 + 940 ps, and t_0 + 950 ps, respectively.

Plasmoid reconnection theory alone is not sufficient to explain the dynamics of the magnetic fields in this experiment. The discontinuities in the dark regions of the film indicate that reconnection may have been inhibited rather than enhanced. A future experiment is required to capture the dynamics in between the time windows captured in this experiment. The laser–plasma interaction is also being investigated using computer simulations.

The experiment was conducted at the Omega Laser Facility with the beam time through NLUF under the auspices of the U.S. DOE/NNSA by the University of Rochester's Laboratory for Laser Energetics under Contract DE-NA0003856.

Achieving Neutron Star Envelope-Relevant Conditions Through a Radiative Shock in a Strongly Coupled Plasma

C. C. Kuranz,* H. J. LeFevre,* S. D. Baalrud, and J. Kinney
Nuclear Engineering and Radiological Sciences, University of Michigan
*Principal Investigators

Compact objects are some of the most extreme environments in the universe. The temperatures and densities inside a neutron star can reach truly extraordinary values of 10^9 K and 10^{14} g/cm^3, respectively, at masses of around one solar mass. This makes these objects extremely small (tens of kilometers diameter), which make them difficult to directly observe.[29] In the envelope of a neutron star, in the more-outer portions, radiation dominates the heat transport, and the plasma is not fully stripped, which makes the opacities difficult to model.[30] The strong ion coupling (with the coupling parameter ~10) is a challenging regime for theory and radiation is not typically considered in these systems.[31] Additionally, the strongly coupled nature of this plasma will affect the contributions of bremsstrahlung to the emissivity and opacity, which is not currently adequately modeled. The dimensionless parameter to determine if a shock is radiative is

$$R_F = \frac{2\sigma T^4}{\rho u_s^3},$$

where σ is the Stefan–Boltzmann coefficient, T is the immediate post-shock temperature, ρ is the mass density, and u_s is the shock velocity. If R_F is greater than or about one, then the radiative energy fluxes are significant in the system and the shock is radiative. The coupling parameter determines if the microphysics or bulk physics drives the evolution of the system and one writes it as

$$\Gamma_{ii} = \frac{q^2 Z^2}{4\pi\varepsilon_0 \bar{d} T},$$

where q is the fundamental charge, Z is the ionization, ε_0 is the permittivity of free space, d is the Wigner–Seitz radius, and T is the plasma ion temperature. If Γ_{ii} is greater than one, then the plasma is strongly coupled.

The SCRaP Campaign addresses these problems with a novel capsule implosion experiment. It uses an 860-μm-outer-diam capsule with a 7-μm outer plastic layer and a mid-Z metal layer on the interior surface. The experiments described here used three capsule designs with three different material layers: 0.2 μm of nickel, 0.4 μm of titanium, or 0.7 μm of aluminum. The different layer thicknesses provide capsules of equal mass, so the drive energy can remain unchanged between the different capsule designs. The drive consisted of 60 beams with SG5-650 phase plates and 1-ns square pulses using about 120 J per beam. This resulted in an average irradiance of 3×10^{14} W/cm^2 over the surface of the capsule. The primary diagnostics used to measure the conditions in these experiments were x-ray framing cameras and a time-integrated spectrometer. The framing cameras used 8× magnification and a 50-ps pulse forming module. The Henway spectrometer uses four convex crystals with image-plate detectors covering a spectral range of about 3 to 13 keV.

Figure 17(a) shows contrast-enhanced framing camera data of a nickel-lined capsule implosion. These images have a pair of 20-μm-thick copper and 12.5-μm-thick nickel foils at the rear filter to act as an imager of K-shell emission from nickel. This makes the images show where only the nickel is during the implosion. The regions labeled 1, 2, and 3 in Fig. 17(a) show the imploding shell, the accretion of matter at the center of the shell, forming a shock, and the shock reaching the plastic resulting in rapid cooling, respectively. Figure 17(b) shows the measured velocity of the rebounding shock as about 180 km/s. Figure 17(c) shows the line emission from the highly ionized Ni and an absorption feature at lower energies due to the absorption of bremsstrahlung produced in the hot, dense core of the capsule implosion along the radial gradient in conditions.

This shock velocity is lower than what 1-D radiation hydrodynamics predict, and 2-D simulations are in progress to determine if structure in the imploding material leads to these effects. Further analysis of the spectra will provide the ionization of the pre-shock material and the volume-averaged density, which will be useful for constraining the dimensionless parameters described above.

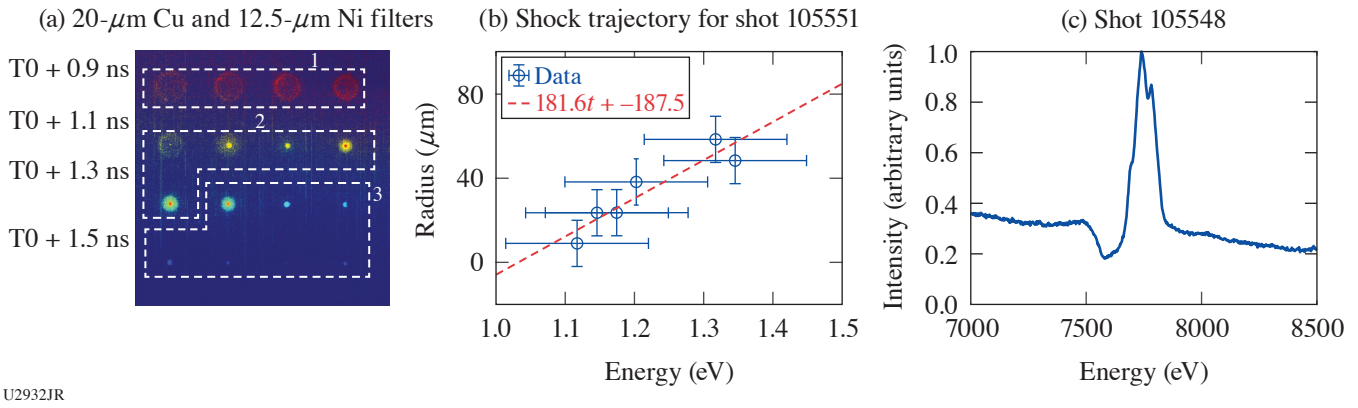

Figure 17
(a) Contrast enhanced framing camera data of a Ni-lined capsule implosion showing region 1 where the Ni shell is imploding and decreasing in radius, region 2 where mass begins accreting at the center of the capsule and forms a rebounding shock, and region 3 where the shock reaches the plastic then expands and cools. (b) The trajectory of the rebounding shock from (a). The linear fit to the data shows a shock velocity of about 180 μm/ns. (c) Spectroscopic data showing the 2 ≥ 1 emission features of Li, Be, and B-like emission features of Ni with an absorption feature to the red of the emission lines due to gradients in the plasma.

This material is based upon work supported by the National Science Foundation MPS-Ascend Postdoctoral Research Fellowship under Grant No. 2138109. This work is supported by SSAA Grant 13432116, and the NLUF Program, grant number DE-NA0002719, and through LLE/NNSA Cooperative Agreement No. DE-NA0003856.

Observation of a Radiative Heat Front in Ar Using the OMEGA Gas-Jet System

C. C. Kuranz,[1*] H. J. LeFevre,[1*] and K. V. Kelso[2]
[1]Department of Nuclear Engineering and Radiological Sciences, University of Michigan
[2]Department of Applied Physics, University of Michigan
[*]Principal Investigators

Radiation from hot, massive stars in star-forming regions can heat the surrounding nebula, heating it and producing an HII region, which consists of ionized hydrogen.[32] This heating propagates as a radiation-driven heat front and this may influence the development of clumps in the nebula, which is an open question in astrophysics.[33,34] The PIonFront Campaign on OMEGA creates a radiative heat front to study the radiation hydrodynamics of this system and understand the ionizing radiation–matter interactions that drive its evolution. The goal of this work is to produce a radiative heat front where photoionization dominates the energy deposition. To determine if that is the case and the front is in the desired physics regime, the dimensionless parameters α and β define the physics regime. The parameter α is the ratio of recombination to photoionization

$$\alpha = \frac{^{n}(\mathrm{i}+1)^{n_\mathrm{e}} R_{\mathrm{i}+1,\mathrm{i}}}{n_\mathrm{i}\Gamma_{\mathrm{i},\mathrm{i}+1}},$$

where n_i is the number density of the ith ionization state, n_e is the electron number density, $R_{\mathrm{i}+1,\mathrm{i}}$ is the recombination rate coefficient, and $\Gamma_{\mathrm{i}+1,\mathrm{i}}$ is the photoionization rate. If α is less than one, then photoionization dominates over recombination. The parameter β is one plus the ratio of electron collisional ionization to recombination

$$\beta = 1 + \frac{n_\mathrm{i}\langle\sigma v\rangle_{\mathrm{i},\mathrm{i}+1}}{n_{\mathrm{i}+1}R_{\mathrm{i}+1,\mathrm{i}}},$$

where $\langle\sigma v\rangle_{\mathrm{i},\mathrm{i}+1}$ is the electron collisional ionization rate coefficient, and all the other values are the same as for α.

To conduct these experiments, it is necessary to have a driving x-ray source and a propagation medium. These experiments use a 500-nm-thick gold foil, irradiated with a 5-ns laser pulse with an irradiance of 10^{14} W/cm^2 to create a bright, quasi-blackbody source. The OMEGA gas-jet system using argon gas with a 2-mm-diam, Mach 5 nozzle and a backing pressure of 750 psi acts as the propagating medium.[35] Figure 18(a) demonstrates the experimental geometry. A capsule implosion using 17 beams with 1-ns square pulses creates a bright, short-lived (~200-ps) probe source for absorption spectroscopy of the argon K shell. The spectroscopic measurement uses a flat, pentaerithritol crystal using an MS image plate as a detector with the backlighter duration self-gating the signal. Figure 18(b) shows the time series of the absorption spectroscopy measurements, indicating a cold plasma with minimal changes to the spectrum until after 2.5 ns after the drive turns on when $n = 1 \rightarrow 3$ and $n = 1 \rightarrow 2$ transitions in argon appear. Additionally, the argon K edge shifts to higher energy due to ionization from the heat front. This indicates a delay in the arrival of the heating at the probe location in the center of the gas jet, 3 mm from the initial driving source position, relative to the speed of light. The appearance of $n = 1 \rightarrow 2$ transitions also indicates that the source ionizes the argon the neon-like state and likely stops at the chlorine-like state. Figure 18(b) shows the time series of spectra over several shots that demonstrates the increase in ionization as the radiative heat front passes the measurement volume.

Currently, the radiation-hydrodynamics simulations of these experiments overpredict the velocity of the heat front. This makes it difficult to compare synthetic spectra to the measured results. Efforts are underway to improve the model of the driving source used in the experiment to address this discrepancy between simulation and experiment. These combined efforts will result in a determination of α and β using the measured and simulated results with models for the atomic rate coefficients.

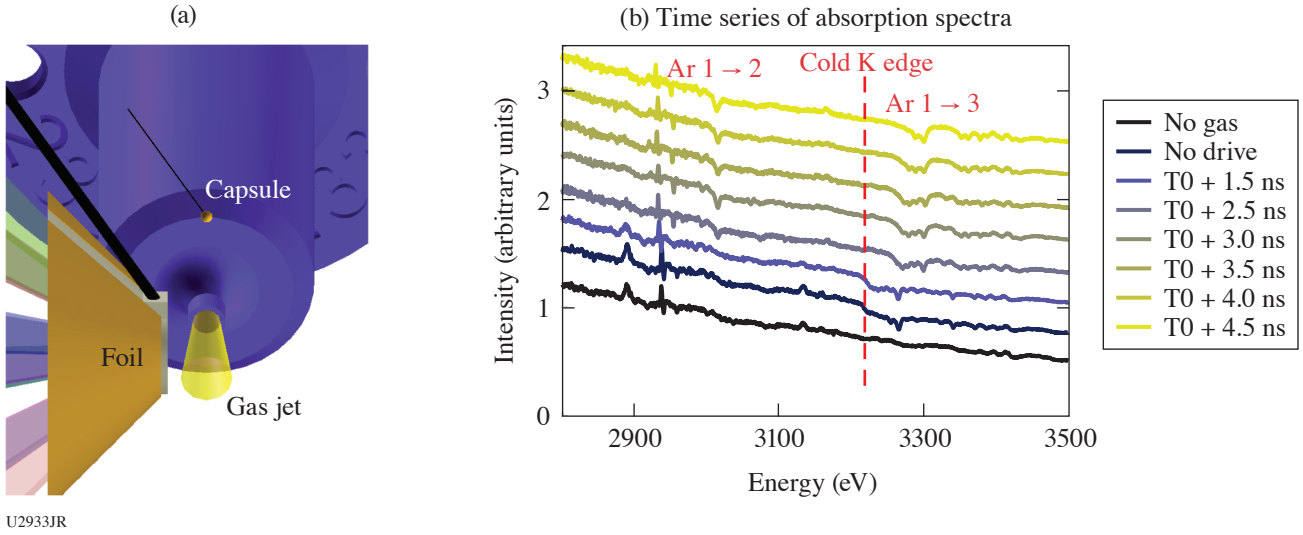

Figure 18
(a) A *VISRAD* model of the gold foil target, the capsule backlighter, and the gas jet. (b) A series of spectra with one spectrum collected during a single shot progressing upward from the bottom. The first (bluest) spectrum is from a capsule backlighter only and the next spectrum has a capsule backlighter with undriven Ar gas. The following spectra moving upward show a delayed onset of a blue shifting of the K edge, which indicates ionization. This is indicative of a heat front propagating through the gas column.

This material is based upon work supported by the National Science Foundation MPS-Ascend Postdoctoral Research Fellowship under Grant 2138109. This work is funded by the U.S. Department of Energy NNSA Center of Excellence under cooperative agreement number DE-NA0003869, and through the LLE/NNSA Cooperative Agreement No. DE-NA0003856.

Onset, Subsistence, and Decay of Magnetized Turbulence and Fluctuation Dynamo

H. Poole,[1] A. F. A. Bott,[1,2] C. A. J. Palmer,[3] Y. Lu,[4] S. Iaquinta,[1] S. Zhang,[1] K. Moczulski,[4,5] P. Farmakis,[4,5] A. Reyes,[4] A. Armstrong,[4,5] D. H. Froula,[5] J. Katz,[5] T. Johnson,[6] C. K. Li,[6] R. D. Petrasso,[6] J. S. Ross,[7] H.-S. Park,[7] P. Tzeferacos,[1,4,5*] G. Gregori,[1] and D. Lamb[8*]
[1]Department of Physics, University of Oxford
[2]Department of Astrophysical Sciences, Princeton University
[3]Centre for Plasma Physics, School of Mathematics and Physics, Queen's University Belfast
[4]Flash Center for Computational Science, Department of Physics and Astronomy, University of Rochester
[5]Laboratory for Laser Energetics, University of Rochester
[6]Plasma Science and Fusion Center, Massachusetts Institute of Technology
[7]Lawrence Livermore National Laboratory
[8]Department of Astronomy and Astrophysics, University of Chicago
[*]Principal Investigators

Magnetic fields are ubiquitous in the universe and are salient agents in numerous astrophysical processes;[36] their origin, however, is not fully understood. Guided by high-fidelity *FLASH*[37,38] simulations, the TDYNO collaboration has conceived, designed,[39] and successfully executed experimental campaigns at the Omega Laser Facility through the NLUF Program that demonstrated turbulent dynamo in the laboratory for the first time,[40] establishing laboratory experiments as a component in the study of turbulent magnetized plasmas.[41] Our more-recent experimental results on OMEGA were able to realize a time-resolved characterization of the evolution of magnetized turbulence in the magnetic Prandtl number (*Pm*) order-unity regime,[42] which is directly relevant to that of idealized fluctuation dynamo simulations and demonstrated the insensitivity of the dynamo achieved in the experiments to initial conditions.[43] The TDYNO platform was also successfully deployed to create an experimental analogue for transport of ultrahigh energy cosmic rays in stochastic magnetic fields.[44] The success of past OMEGA campaigns enabled the launch of a concerted effort to study and characterize turbulent dynamo in various plasma regimes and for different astrophysical environments, springboarding sister experimental campaigns at world-class laser facilities. Using large-scale *FLASH* simulations, we ported the TDYNO platform to the National Ignition Facility at Lawrence Livermore National Laboratory, where the hundredfold increase in available energy enabled us to demonstrate turbulent dynamo in a regime relevant for magnetized turbulence in galaxy clusters. The strong magnetization of the turbulent plasma resulted in prominent reduction of local heat transport and highly structured temperature distributions[45] seen in intracluster medium plasmas and explaining hot galaxy cluster cores. In experiments at the French Laser Mégajoule Facility (the first academic experiment there) we demonstrated, for the first time, magnetic-field amplification in supersonic turbulence[46] relevant to the star-forming interstellar medium. As a result, we can now critically assess dynamo theory and numerical predictions through dedicated experiments with the TDYNO platform. Under the auspices of the NLUF Program, we are building on our recent work and achievements, and are executing an experimental campaign on OMEGA to answer key fundamental questions pertinent to the onset, subsistence, and decay of magnetized turbulence and turbulent dynamo: (1) What is the range of critical magnetic Reynolds numbers for the onset of subsonic fluctuation dynamo in the *Pm* order-unity regime, where most resistive-MHD driven-turbulence simulations in the literature lie? (2) How does the magnetic energy of the saturated dynamo state depend on *Pm*? Can we reach larger magnetic fields if high plasma temperatures are sustained? (3) How, why, and at what rate do magnetized turbulence and its magnetic energy decay?

The first shot day of our ongoing OMEGA campaign was carried out 3 June 2022 and was geared toward measuring the decay rate of magnetized turbulence and characterizing the dissipation of magnetic energy at late times, i.e., question 3 above. To date, our OMEGA experimental campaigns have focused on the onset and saturation of the fluctuation dynamo mechanism but have not studied how the magnetic energy and plasma turbulence eventually decay. While the hydrodynamic case of how the kinetic energy decays was solved by Kolmogorov[47] in 1941, theories for the decay of nonhelical stochastic magnetic fields have only recently been proposed, predicting specific decay power laws ($\propto t^{-10/9}$ and $\propto t^{-20/17}$ in the fast- and slow-reconnection regimes, respectively). The platform deployed is shown in Fig. 19(a) and is similar to the one we fielded on OMEGA for our previous successful TDYNO campaigns[42] with diagnostics trained at late times of the plasma evolution. The assembly is comprised of two composite targets and two grids that are connected by a pair of cylindrical shields. The composite targets are 3 mm in diameter and consist of a 50-μm-thick polystyrene foil (CH) and a 230-μm-thick polystyrene washer. The polystyrene

washers were machined to have a 400-μm-diam cylindrical "well" in their centers. The two targets are mounted 8 mm apart and the pair of grids is placed between them. The two grids are made of polyimide and are mounted 4 mm apart—each of them 2 mm away from the respective proximate face of the foil target. The grids have a diameter of 3 mm, a thickness of 250 μm, and consist of 300-μm-wide holes and 100-μm wires, offset with respect to each other to break the mirror symmetry of the assembly: grid A (red) has a hole in the center, while grid B (blue) does not. Rectangular cones on each target shield the diagnostics from the intense x-ray emission produced when a sequence of ten 1-ns-duration laser beams coming from different angles illuminate each target. The two targets are driven for 10 ns, delivering a total of 5 kJ per target on an area defined by the laser SG5 phase plates. The temporal profile of the drive is a flattop profile. As shown in the *FLASH* simulation we performed for the platform design, the beams drive a pair of counter-propagating, high-magnetic Reynolds number *Rm*, plasma flows that carry the seed magnetic fields generated by Biermann battery. The flows propagate through a pair of grids [Fig. 19(b)] that destabilize the flow and define the driving scale of the turbulence (*L*). The flows then meet at the center of the chamber to form a hot, turbulent interaction region where the magnetic fields are amplified to saturation values [Fig. 19(c)].

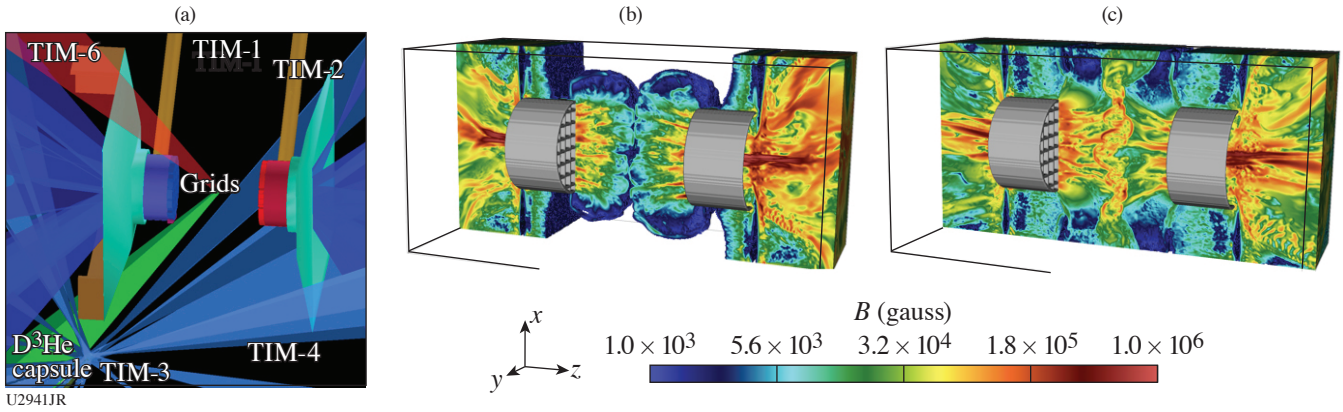

Figure 19
Turbulent dynamo experiments on OMEGA. (a) *VISRAD* schematic of the TDYNO platform for OMEGA to study the decay of the turbulence and its kinetic and magnetic energy. (b) *FLASH* simulation of experiment showing the flows carrying seed magnetic fields to the center where the turbulent interaction is established. (c) Same as (b) but after the establishment of the turbulent interaction region. There, fluctuation dynamo action amplifies the magnetic fields to saturation values prior to their subsequent decay at $t > 30$ ns.

To fully characterize the properties of the magnetized turbulent plasma at late times (>28 ns after the laser drive), we fielded our mature suite of experimental diagnostics [Fig. 19(a)] that consists of (1) an x-ray framing camera (TIM-1: XRFC3) to measure the x-ray fluctuations [Fig. 20(a)] associated with the turbulent spectrum; (2) the 4ω optical Thomson-scattering diagnostic (TIM-4: alignment cart and TIM-6: collection cone) to characterize plasma temperatures, density, and velocities by measuring the ion-acoustic wave (IAW) signal and the electron plasma wave (EPW) signal; and (3) proton radiography (TIM-3: target positioner for the D^3He capsule and TIM-2: CR-39 film pack) to record the 3-MeV and the 15-MeV [Fig. 20(b)] protons generated by the implosion of a D^3He MIT capsule, which are subsequently deflected by the stochastic magnetic field of the turbulent plasma. The proton radiographs are being post-processed to recover the path-integrated magnetic-field maps using the inversion techniques we developed.[8]

The shots yielded a wealth of experimental data and preliminary analysis indicates that we were in fact able to capture the decay rates of the turbulence. The temporal decay of the x-ray intensity fluctuations, and therefore in the turbulent kinetic energy, is clearly visible in the x-ray images we recorded [Fig. 20(a)]. Moreover, the 4ω Thomson-scattering diagnostic (not shown) yielded detailed information on the plasma state (ion and electron temperatures, bulk flow velocity, turbulent velocity, and electron density). Finally, the proton-radiography diagnostic performed perfectly, and the magnetic-field decay was captured in a sequence of proton radiographs [Fig. 20(b)]. We are grateful to the MIT team for their careful etching and development. In the radiographs, we see the gradual reduction in time of the stochastic features but also a reduction in their sharpness, both indica-

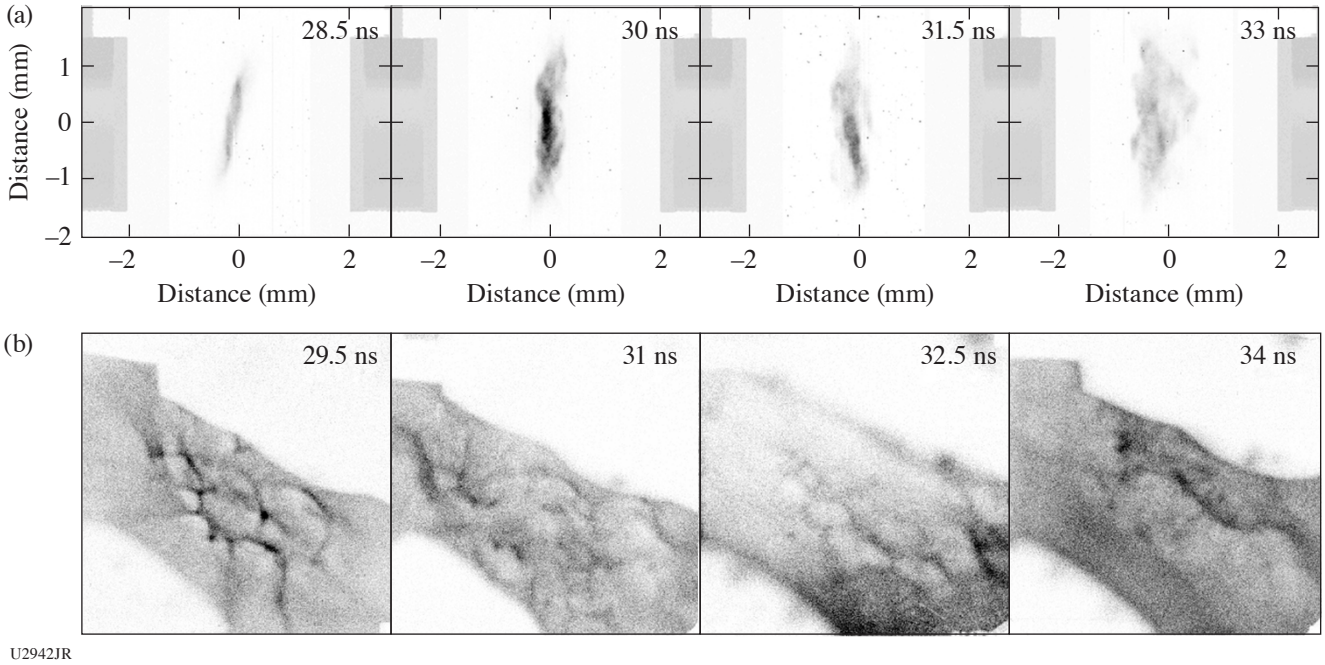

Figure 20

Experimental results. (a) Self-emission x-ray images of the turbulent interaction region from the 2× magnification framing camera at 28.5 ns, 30 ns, 31.5 ns, and 33 ns. The images were taken using a mylar-vanadium filter and can also be used to recover electron temperature information using the method we developed for our National Ignition Facility campaign.[45] Both emission and stochastic features decay in time, which can furnish the decay rate for the kinetic energy. (b) Late-time 15.0-MeV proton images of interaction-region plasma. The D^3He capsule is imploded using 17 270-J beams, each with a 600-ps pulse length and 1.82-mm defocus. This results in the generation of ~109 3.3- and 15.0-MeV protons via nuclear fusion reactions. These protons pass through the stochastic magnetic field and are deflected before reaching the CR-39 detector. The proton images are now being post-processed to recover path-integrated magnetic-field measurements[8] that will quantify the decay rate of the magnetic energy. The gradual reduction in time of the stochastic features and their sharpness is visible, indicative of magnetic energy decay.

tive of a measurable reduction in magnetic energy values. The quantitative analysis of these results will furnish the decay rates that we sought to characterize in this shot day. Despite the complexity of the experimental platform, with the help of personnel from the Laboratory for Laser Energetics, we were able to perform 12 shots during our first shot day. The experimental data are currently being analyzed and promise to further our understanding of how astrophysical magnetized turbulence decays.

The research leading to these results received funding from the U.K. EPSRC (grant numbers EP/M022331/1 and EP/N014472/1); the European Research Council under the European Community's Seventh Framework Programme (FP7/2007-2013)/ERC grant agreements nos. 256973 and 247039; the U.S. DOE under Contract No. B591485 to LLNL; Field Work Proposal No. 57789 to ANL and Awards DE-SC0016566, DE-NA0003605, and DE-NA0003934 to the University of Chicago; DE-NA0003868 to the Massachusetts Institute of Technology; DE-NA0001808, 89233118CNA000010, and 89233119CNA000063 to General Atomics; subcontract nos. 536203 and 630138 (LANL) and B632670 (LLNL) and Award DE-SC0021990 to the Flash Center for Computational Science, University of Rochester; and Cooperative Agreement DE-NA0003856 to the Laboratory for Laser Energetics (LLE), University of Rochester. LLNL work was performed under the auspices of the U.S. Department of Energy by Lawrence Livermore National Laboratory under Contract DE-AC52-07NA27344. We acknowledge support from the NSF under grants PHY-1619573 and PHY-2033925. Awards of compute time were provided by the U.S. DOE ALCC program. Compute time was provided by the U.S. DOE ALCC and ERCAP programs, and the LLE High-Performance Computing group. We acknowledge funding from grants 2016R1A5A1013277 and 2020R1A2C2102800 of the NRF of Korea. Support from AWE plc. and the STFC of the UK is also acknowledged. The Omega shots were allocated through the U.S. DOE NNSA NLUF Program at LLE. The software used in this work was developed in part by the DOE NNSA- and DOE Office of Science-supported Flash Center for Computational Science at the University of Chicago and the University of Rochester.

Collision of Magnetized Jets Created by Hollow Ring Lasers Irradiating High-Z-Doped CH Targets

E. P. Liang,[1*] L. Gao,[2,3] and H. Ji[2,3]
[1]Rice University
[2]Princeton University
[3]Princeton Plasma Physics Laboratory
[*]Principal Investigator

In our 2022 NLUF experiment we investigated the effects of radiative cooling on magnetized, high-beta shocks by colliding head-on two supersonic magnetized jets created by irradiating Fe-doped flat CH targets using a hollow ring of laser beams.[48,49] In earlier OMEGA experiments we successfully demonstrated the creation of such shocks with two opposing jets by using 19 beams from each hemisphere of OMEGA to irradiate flat pure CH targets in a hollow ring pattern. We have characterized the properties of these magnetized jets and shocks and investigated the role of electron thermal conductivity. In the 2022 experiment we explored the effects of radiative cooling by adding 1% to 2% (atomic) Fe dopants to the CH targets to increase the radiative cooling and systematically compare the results with those from pure CH targets. This project is in progress since we only received the first half of proton radiography (Prad) data from MIT at the writing of this report. The preliminary data from all diagnostics appear excellent. We are confident of achieving our original scientific objectives. Our next experiment of this NLUF project, currently scheduled for May 2023, will use Sn-doped CH targets to further increase the effects of radiative cooling. The final results of both experiments will have broad applications to magnetized radiative shocks in both astrophysics and magnetized high-energy-density science, including magnetized ICF.

Experiment Setup and Diagnostics

In the 27 April 2022 experiment, 19 beams from each hemisphere of OMEGA were configured to form an 800-μm-radius hollow ring pattern, irradiating a 1% to 2%-Fe-doped flat CH disk. Two such disks face each other at a separation of 6.4 mm. MG magnetized jets launched from each target collide head-on at mid-plane centered near target chamber cebter (TCC). Strongly magnetized shocks were created and propagated upstream into the jet body. Radiative cooling from the Fe dopants is expected to affect the magnetic-field strength, electron transport, and shock strength, structure, and evolution. We plan to systematically compare the results of Fe-doped CH targets with those of pure-CH targets to quantify the effects of high-Z dopants and compare with 3-D *FLASH* simulation results. The primary diagnostics are the same as those used in our earlier experiments: Thomson scattering (TS) at both TCC and off-TCC locations, x-ray framing camera time-lapse x-ray imaging, and proton radiography using D^{3}He protons for OMEGA shots. Figure 21 is a sketch of the experimental setup and diagnostics.

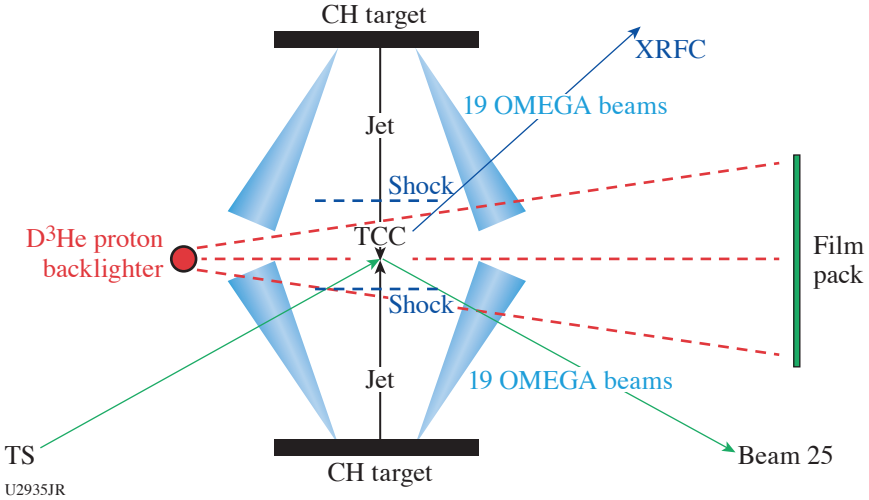

Figure 21
Sketch of experimental setup of colliding MG jets experiment using 38 OMEGA beams to irradiate two opposite flat CH disks separated by 6.4 mm. Locations of the main diagnostics are also indicated. In the 2022 experiment the CH disks were doped with 1% to 2% (atomic number) Fe.

Preliminary Results of the 220427 Experiment

We successfully completed nine shots on 27 April 2022 and obtained excellent data from all three diagnostics. Sample data are shown below even though we have not had the time to complete the detailed analysis, modeling, and comparison with earlier experiments. These tasks are in progress.

Figure 22 shows Prad images that are consistent with the conceptual picture of strong poloidal fields parallel to the jet axis, while strong transverse fields are created and amplified near the contact surface by the collision. Even though these images resemble those of earlier experiments with pure-CH targets, we expect the detailed field configurations and evolution will vary with radiative cooling. This will be investigated after the fields are fully deconvolved from the Prad images and compared with 3-D *FLASH* simulations, which are ongoing. The magnetic fields will strongly impact electron thermal conduction.

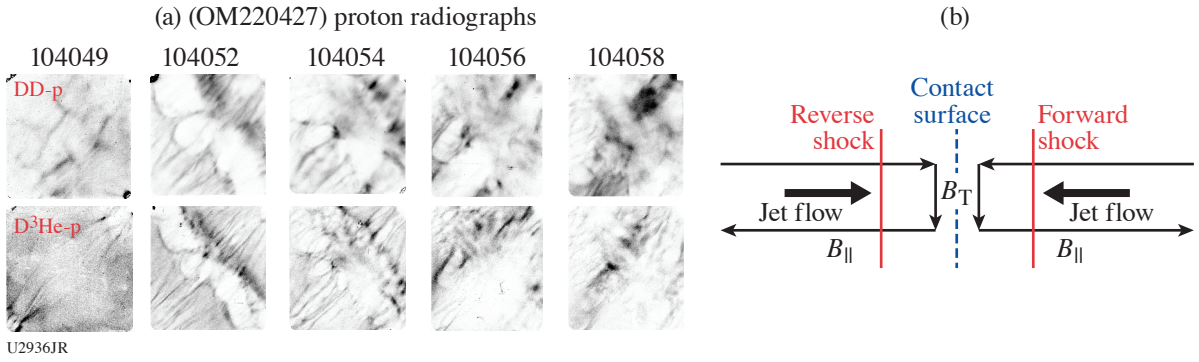

Figure 22
(a) Prad images of the 220427 experiment showing the evolution of ordered poloidal fields along jet axis and transverse fields along the contact surface, consistent with the conceptual picture below. Jet axis lies at 45° from lower left to upper right.

Figure 23 compares the TS data at TCC from 2021 (pure-CH) and 2022 (Fe-doped) experiments. They suggest that the electron temperature and density are lower, but the ion temperature and flow velocity are higher in the Fe-doped cases. These results will be compared with 3-D *FLASH* results before we can provide physical interpretations because the effects of radiative cooling are complex and highly nonlinear. All these results will be used to design and optimize our next NLUF experiment scheduled for May 2023.

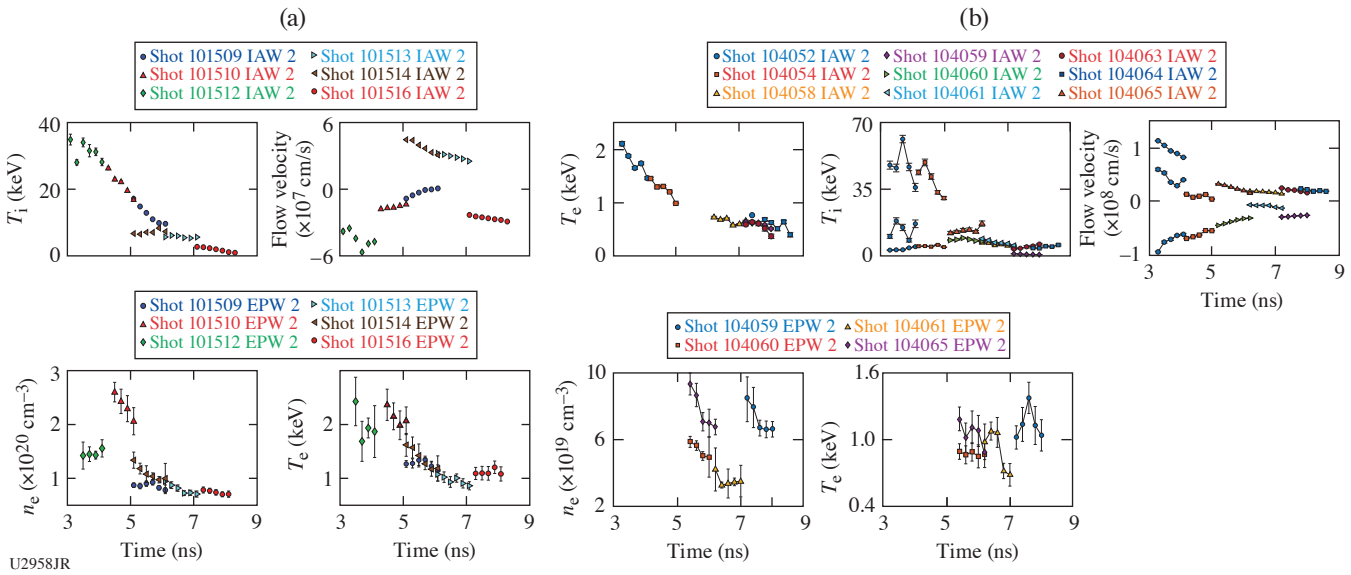

Figure 23
Comparison of TS data at TCC from (a) 210811 (pure CH) and (b) 220427 (Fe-doped CH) show that T_e and n_e are lower, while T_i and flow velocity are higher, for the Fe-doped targets.

Rice University graduate students Yingchao Lu (Ph.D., 2021, current University of Rochester postdoc) and Brandon Cage (second year) and undergraduate student Jackson White (BS, 2021), Princeton University graduate student Abe Chen and postdoc Sue Zhang, contributed to these experiments.

This work was supported by DOE DE-NA0003942.

X-Ray Heating and Ionization of Photoionized Plasmas in Steady State

R. C. Mancini,[1*] R. F. Heeter,[2] D. Liedahl,[2] and S. P. Regan[3]
[1]University of Nevada, Reno
[2]Lawrence Livermore National Laboratory
[3]Laboratory for Laser Energetics, University of Rochester
[*]Principal Investigator

The goal of this project is to study the x-ray heating, temperature, and ionization properties of plasmas produced and sustained by a broadband intense x-ray flux, i.e., photoionized plasmas, with experiments on OMEGA EP. Most laboratory work performed to date on high-energy-density laboratory physics pertains to collisional plasmas, i.e., plasmas where electron collisional processes play a dominant role in the plasma ionization and atomic physics. Relatively little attention has been paid, however, to studying and understanding the basic properties of laboratory photoionized plasmas where both photoionization and photoexcitation, driven by an external broadband x-ray flux, become dominant. These relatively low-density plasmas are important for understanding a myriad of astrophysical phenomena including x-ray binaries, warm absorbers in active galactic nuclei, and the accretion disks formed in the vicinity of compact objects. The quantitative information that we obtain from these systems is mainly based on the analysis of x-ray astronomy observations made by orbiting telescopes such as Chandra and XMM-Newton.

Given the time scales of astrophysics phenomena, the models implemented in astrophysical codes assume that the plasma is in steady state. In the case of photoionized plasmas, the type of steady state is photoionization equilibrium (PIE), where photon-driven photoionization is counterbalanced by electron-driven radiative and dielectronic recombination. Achieving PIE in the laboratory is challenging since it requires large driver energy and long times. We have established a new experimental platform on OMEGA EP that uses a plastic-tamped silicon sample driven by the 30-ns-duration, broadband x-ray flux produced by the "Gatling-gun" radiation source. This source is comprised of three copper hohlraums that are sequentially driven by three OMEGA EP beams, each one delivering 4 kJ of UV energy in a 10-ns square pulse shape. Each copper hohlraum has a length of 2.8 mm and an inner diameter of 1.4 mm, and is filled with TPX foam. The laser beams sequentially illuminate one hohlraum at a time, thus producing an x-ray flux characteristic of 90-eV radiation temperature for a time of 30 ns. The relatively long duration of the Gatling-gun radiation source is critical to produce a photoionized in steady state. The experiment setup is schematically illustrated in Fig. 24.

The experiment employs the four OMEGA EP beams and has three target components. Beams B3, B2, and B4 sequentially drive the "Gatling-gun" (GG) x-ray source. Each of these beams lasts for 10 ns. The 30-ns-duration x-ray flux of GG irradiates the photoionization sample, i.e., a plastic-tamped SiFe or SiO foil, to produce a photoionized plasma that undergoes a controlled expansion. Beam B1 is independently fired to drive a Ti laser-produced plasma source of backlit photons to probe the photoionized plasma at different times in nominally identical shots via transmission spectroscopy. This laser beam is 1 ns long and delivers 1 kJ of UV energy onto a Ti slab target in a 1-ns square pulse shape. The radiative recombination continuum emission photons of the Ti laser-produced plasmas backlight and probe the photoionized plasma via K-shell absorption spectroscopy. From this measurement, the charged-state distribution and electron temperature of the plasma can be extracted.

The combination of a 30-ns-long x-ray flux to produce and sustain the photoionized plasma and the possibility of performing transmission spectroscopy with a relatively short duration (i.e., 1-ns) source of backlit photons is key to demonstrating that the plasma is in steady state. In addition, gated imaging measurements of the plasma self-emission provide the density of the plasma. The GG performance is monitored with a VISAR package located on the back end of GG and the active shock breakout (ASBO) and SOP diagnostics, as well as a grating spectrometer to record the broadband spectral distribution GG x-ray flux. The GG x-ray source has a characteristic radiation temperature T_R = 90 eV and lasts for 30 ns.

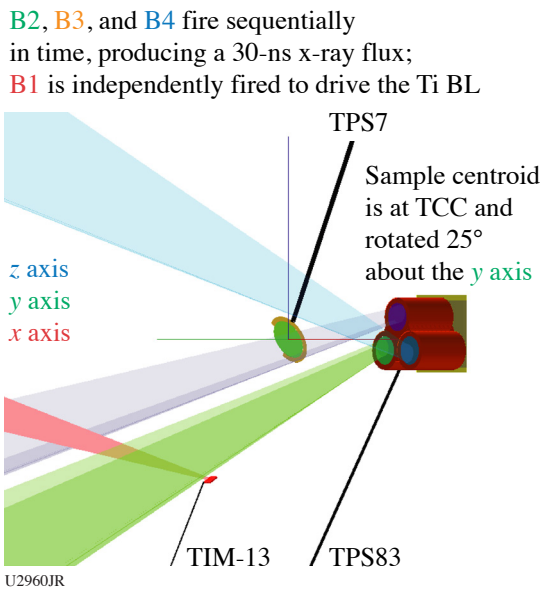

Figure 24
Schematic of the experiment setup. OMEGA EP beams B3, B2, and B4 fire sequentially in time to drive the three-hohlraum Cu Gatling-gun x-ray source, producing a 30-ns x-ray flux, while beam B1 is independently fired to drive the Ti backlight source. Details of Target Positioning Systems (TPS), TIM's, and diagnostics used in the experiment: TIM-10: SSCA/SXS streaked spectrometer for K-shell transmission spectrum of Si plasma; TIM-11: XRFC5/VSG_1 (variable speed grating) gated spectrometer for Cu x-ray flux; TIM-12: ASBO and SOP diagnostics for VISAR hohlraum radiation temperature; TIM-13: Ti backlighter (BL); TIM-14: SFC1 (Sydor framing camera 1)/VSG_2 gated spectrometer for imaging Si L-shell emission spectroscopy.

The spatial extension of the blowoff TPX/copper plasma from the copper hohlraums is monitored with the 4ω probe laser to make sure that it does not reach the silicon sample. The silicon photoionized plasma is probed with self-emission spectra recorded with a grating spectrometer, and K-shell line absorption spectra are recorded with a KAP crystal streaked spectrometer.

Figure 25 displays measurements recorded in three nominally identical OMEGA EP shots, i.e., 32980, 32981 and 32982, where the Ti backlighter was fired at three different times to monitor the evolution of the plasma-charged distribution via transmission spectroscopy. Everything else in the experiments remained the same. The earliest observation at t = 8 ns shows weak n = 1 to 2 line absorption in F- and O-like Si ions and n = 1 to 3 in Ne-like Si; this indicates that the Si ionization is just breaking into the L-shell range of ions. Later in time, at t = 18 ns and t = 25 ns, the transmission spectrum is dominated by n = 1 to 2 in Ne transitions in F-, O-, N-, and C-like Si ions and it is very similar at both times. This is an indication that the charge-state distribution is the same and thus in steady state. These observations are the first experimental evidence of having achieved a steady-state charged-state distribution in a laboratory photoionized plasma, i.e., PIE.

Shock-Induced Hydrogen Chemistry for Hydride Formation

S. Pandolfi,[1] C. Mcguire,[2] R. Smith,[2] M. C. Marshall,[3] D. Kraus,[4] W. Mao,[5*] A. Gleason,[1] and J. H. Eggert[2]
[1]SLAC National Accelerator Laboratory
[2]Lawrence Livermore National Laboratory
[3]Laboratory for Laser Energetics, University of Rochester
[4]University of Rostock
[5]Stanford University
[*]Principal Investigator

Recent work showing diamond formation in nonreactive polymers under laser-driven compression[50–52] has demonstrated that it is possible to initiate and characterize controlled reactive chemistry over ultrafast (i.e., nanosecond) time scales. Here, we use a novel approach that builds on previous work to: (a) extend previous studies to low-entropy pathways at multi-Mbar pressures; and (b) use shock-induced polymer dissociation and diamond formation as a source of reactive hydrogen (H) atoms to initiate reactive chemistry and hydrides formation.

In this experiment, we used a new sample fabrication procedure that has been recently developed by part of the group, and that allows us to embed particles of selected heteroatoms, in this case iron (Fe), in a polymer matrix, specifically Stycast epoxy.[53] This sample design ensures that, as the dissociation of the polymer takes place under dynamic compression, the heteroatoms are

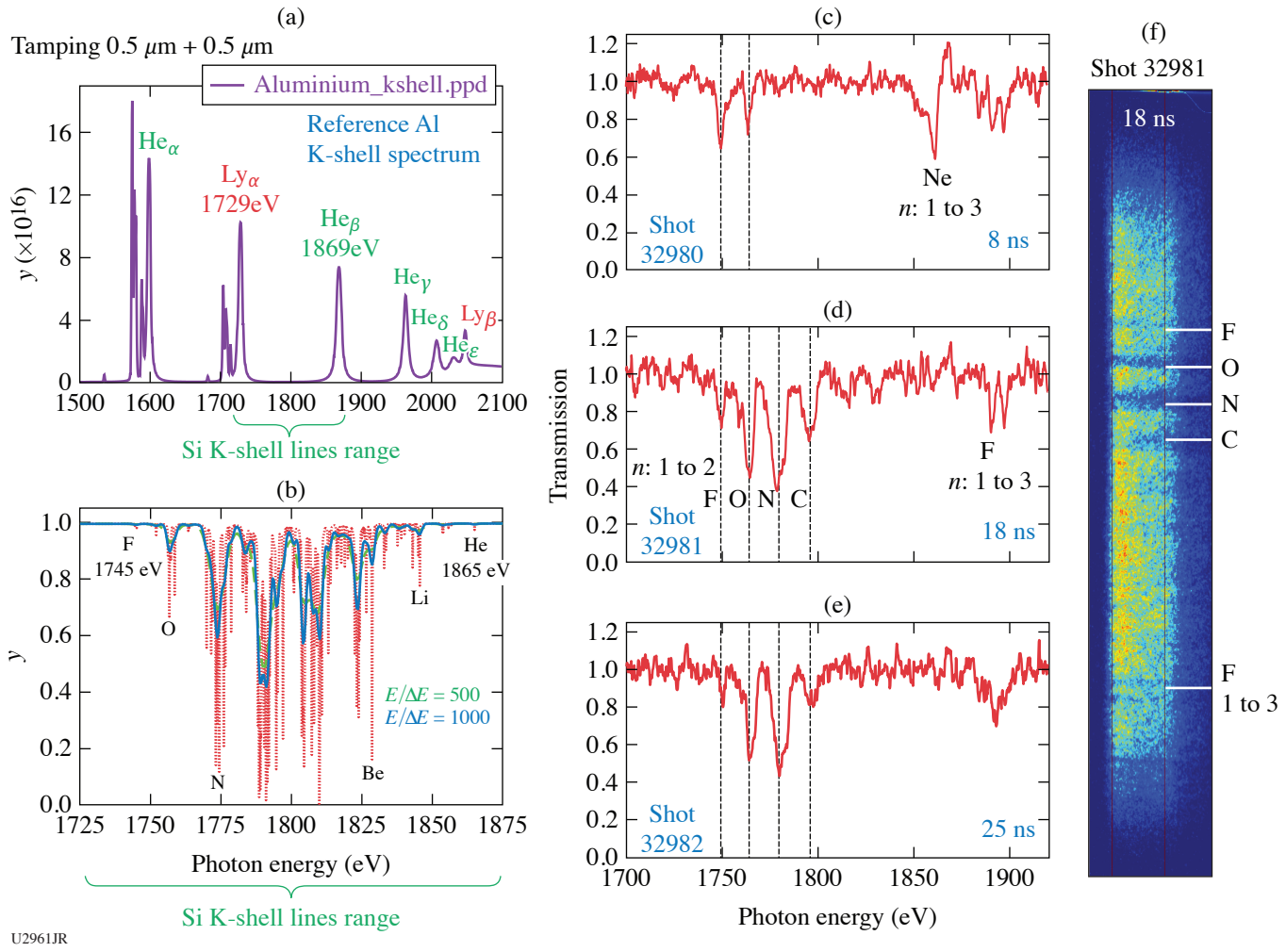

Figure 25

(a) Reference Al K-shell line emission spectrum used to calibrate the photon energy axis, (b) range of Si K-shell line absorption spectrum bounded by the Al Ly_α and He_β lines, and [(c)–(e)] experimental transmission from three nominally identical experiments using 0.5-μm plastic-tamped samples that show steady-state charged distribution in the Si photoionized plasma at t = 18 ns and t = 25 ns (right). (f) The image data is the streaked spectrum recorded with TIM-10/streaked x-ray camera A/streaked x-ray spectrometer (see Fig. 24) from which the transmission is extracted.

surrounded by a carbon- and H-rich environment, promoting eventual chemical reaction. We used the PXRDIP diagnostic and a Fe backlighter to collect x-ray diffraction (XRD) data to characterize the structural evolution of the sample as it undergoes compression; changes in the structure and eventual chemical reaction leading to hydride (or carbide) formation can be readily detected by studying the arrangement of the Fe atoms. Results from our first day of experiments are reported in Fig. 26.

Data analysis shows that single-shock compression yields to polymer dissociation and crystallization of the FeH hydride with double hexagonal close-packed (dhcp) structure [Fig. 26(b)]. This structure differs from the stable one for pure Fe, i.e., a hcp (hexagonal close-packed) structure, demonstrating that the mobility and energy of the H atoms released by polymer dissociation is sufficient to extensively react with the embedded Fe particles. Data collected under ramp compression (i.e., isentropic, low-entropy compression pathways) show a markedly different pattern, compatible with pure hcp Fe, and no signature of diamond formation. This result and other runs performed on pure epoxy show that the low-energy pathways achievable under ramp compression do not lead to diamond crystallization, most likely due to energetic barriers. During FY23, our efforts will focus on exploiting the pulse-shaping capabilities on OMEGA EP to realize a combined shock + ramp compression profile. The initial shock-compression will provide the necessary energy to initiate polymer decomposition, while the following ramp compression will allow us to characterize the hydrides forming at multi-Mbar pressure.

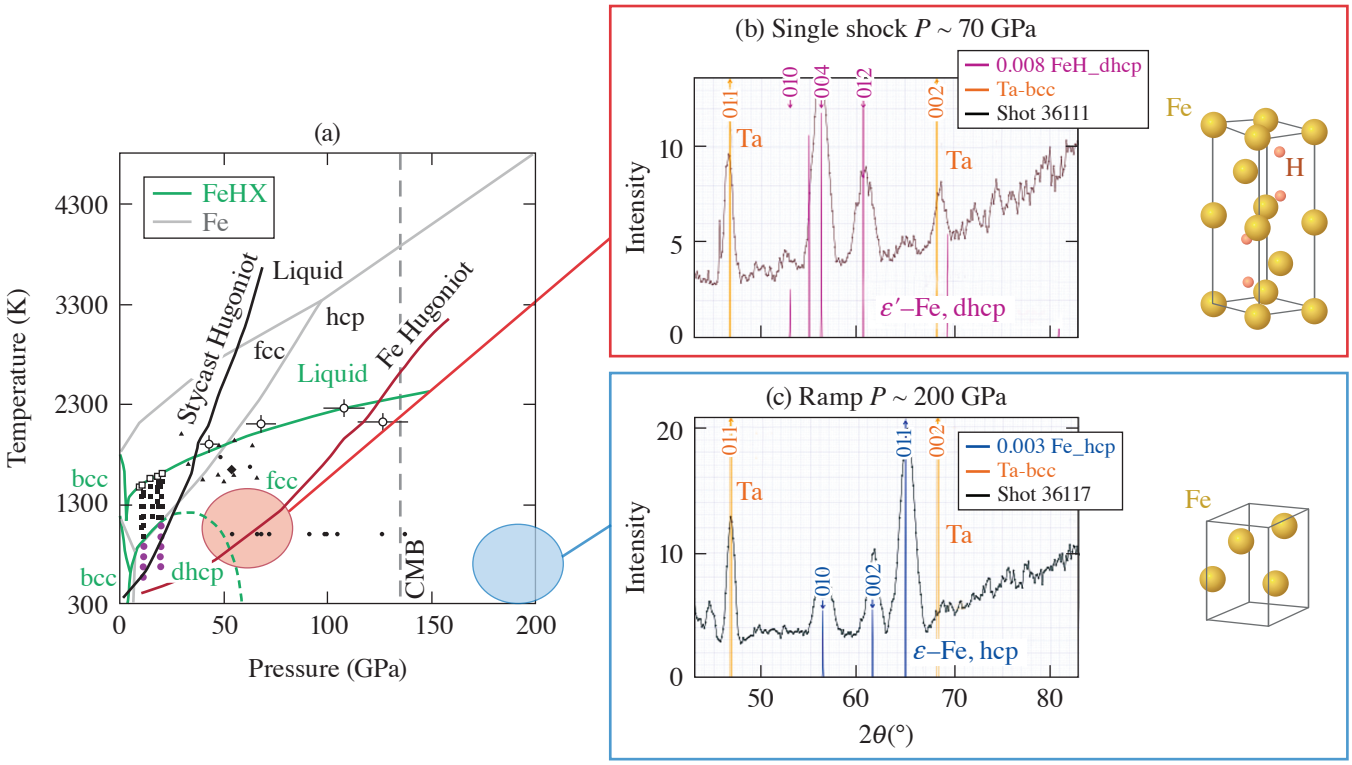

Figure 26
XRD diffraction data collected using different compression profiles. (a) Phase diagram of Fe and iron hydrides, shown in gray and green, respectively, are overlaid with the Hugoniot curve for both pure Fe (red) and pure Stycast. Data obtained using (b) single-shock compression up to 70 GPa and (c) low-entropy ramp compression up to 200 GPa. bcc: body-centered cubic; fcc: face-centered cubic; CMB: core mantle boundary.

Furthermore, part of the experimental time has been dedicated to velocimetry studies to better characterize the samples' equation of state. With a specific target design, we have been able to simultaneously measure our samples and a known material used as reference, quartz in this case, as shown in Fig. 27. The results will be used to further refine the equation of state of the epoxy–Fe mixture and to inform theoretical models investigating epoxy–metal mixtures.

This work is funded through the NLUF Program at LLE. Parts of this work was performed under the auspices of the U.S. Department of Energy by Lawrence Livermore National Laboratory under Contract DE-AC52-07NA27344 and was supported by the LLNL-LDRD Program under Project No. 21-ERD-032. Travel was partially funded by the 2019 DOEFES ECA.

Driving Iron to Dense, Hot Conditions Using Long- and Short-Pulse Beams of OMEGA EP

C. McGuffey,[1*] M. A. Meyers,[2] F. N. Beg,[2] G. Righi,[2] A. Li,[2] M. Bailly-Grandvaux,[2] and J. Kim[2]
[1]General Atomics
[2]University of California, San Diego
[*]Principal Investigator

Iron is an abundant constituent of all burning stars. The opacity of iron is a critical parameter to the inner workings of sun-like stars, constraining the radiative flux leaving the interior, and thus the temperature and nuclear reaction rates. A material's opacity, κ_ν, at a certain frequency, ν, is defined such that

$$I(x) = I_0 e^{-i\kappa_\nu \rho x},$$

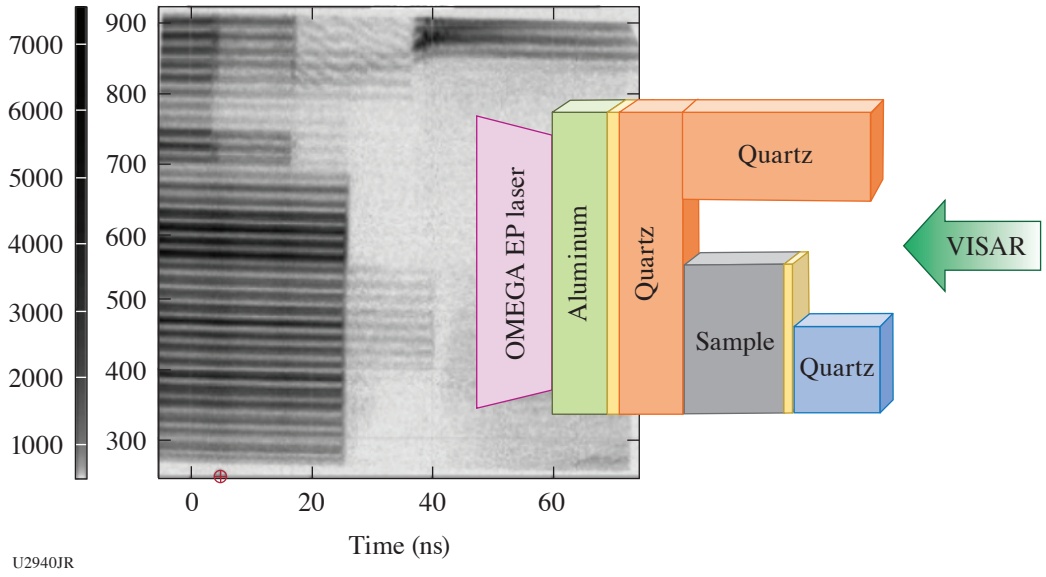

Figure 27
Velocimetry data obtained using the active shock breakout diagnostic and schematic view of the target assembly designed for equation-of-state measurements.

where $I(x)$ is the intensity, lower than the incident intensity I_0, after traveling a distance x through the material with mass density ρ. Opacity is cumulative of multiple contributions. For the materials present in high-energy-density (HED) systems, which are hot and partially or highly ionized, photoelectronic absorption develops multiplicity for all the ionic states present; Doppler broadening and continuum-lowering effects may be present, for example. High-atomic-number, opacity calculations can become intractable, even with large computational resources. This is to say that HED opacity is highly situationally dependent and challenging to model. That is why experimental opacity measurements are important, and in highly radiative HED systems including stars, hohlraums, and ICF capsules, opacity measurements are needed in a variety of conditions.

The FeHotCompress experiment, allocated through the NLUF Program, seeks a methodology for creating dense, hot Fe samples and measuring their opacity on the OMEGA EP Laser System. The methodology combines two common uses of large laser facilities: laser compression[54] and isochoric heating from a laser-driven proton beam.[1,4,55] Laser-direct-drive compression of planar materials has been used to apply well-controlled, high pressure on materials for decades, pushing beyond what diamond-anvil cells can do to study material properties at high pressure. When compressed by an appropriate ramp pulse shape, high density can be attained with minimal temperature increase. Separately, short-pulse laser drivers or the charged-particle beams they create can heat samples quickly enough for the material to retain its initial density ("isochorically"). This dual-drive approach provides flexibility in the conditions that can be attained and could offer a high data collection rate compared to other major iron opacity campaigns using flagship x-ray drivers.

In the FeHotCompress configuration, long-pulse beams irradiate an iron sample package using distributed phase plates for broad, quasi-1-D drive. Short-pulse Beam 1 irradiates a curved plastic foil to direct protons into the sample. Short-pulse Beam 2 serves as an x-ray continuum backlighter with a bare Ti wire target. The objective of the campaign is to collect absorption spectra of Fe in a hot, compressed condition. On the first shot day, x-ray signatures of the three beam types were collected, one by one, using two x-ray spectrometers, which presented challenges. The proton spectrum was recorded for future use in simulations of the target heating. Streaked, spectrally resolved x-ray emission measurements were also taken with the PJ-X streak camera + streaked x-ray spectrometer diagnostic. Figure 28 shows these data for a two-beam shot.

We acknowledge travel support to participate in this shot day provided by the National Nuclear Security Administration. Three students participated in the shot day.

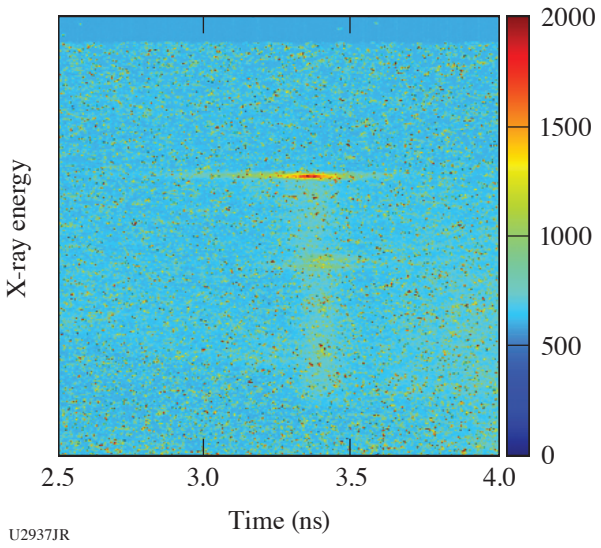

Figure 28
Streaked and spectrally resolved x-ray emission above 5.5 keV from Fe driven by a long-pulse beam and Ti irradiated by a short-pulse beam. Cold and hot Fe lines are seen late in the drive, as is a continuum from the short pulse arrival at 3.4 ns.

Tracking Rarefaction with Particle Image Velocimetry

J. Shang,[1,2*] H. Aluie,[1,2] D. N. Polsin,[1,2] and R. Betti[1,2]
[1]Department of Mechanical Engineering, University of Rochester
[2]Laboratory for Laser Energetics, University of Rochester
[*]Principal Investigator

Prior OMEGA experiments of a plasma releasing into a vacuum suggested that the released material travels more than twice the distance and spreads over 4× the range predicted by radiation-hydrodynamic codes, which could account for a reduction in target performance by a factor of 2 (Ref. 56). In this campaign, we sought to measure the evolution of the rarefaction wave from the leading to the trailing edge by imaging the position of particles embedded in the rear surface of an irradiated CH foil. At shock breakout, the particles would become entrained and move with the fluid.

In the experiment, we used titanium microspheres as the tracer particles and a framing camera to capture the backlit samples over time. A representative sequence of radiographs from the same shot is shown in Fig. 29, where the three particles can be seen in most frames as dark ellipsoids. After release, the particles appear to compress and then expand. Due to this expansion, it is not evident from the images whether the particles have moved appreciably.

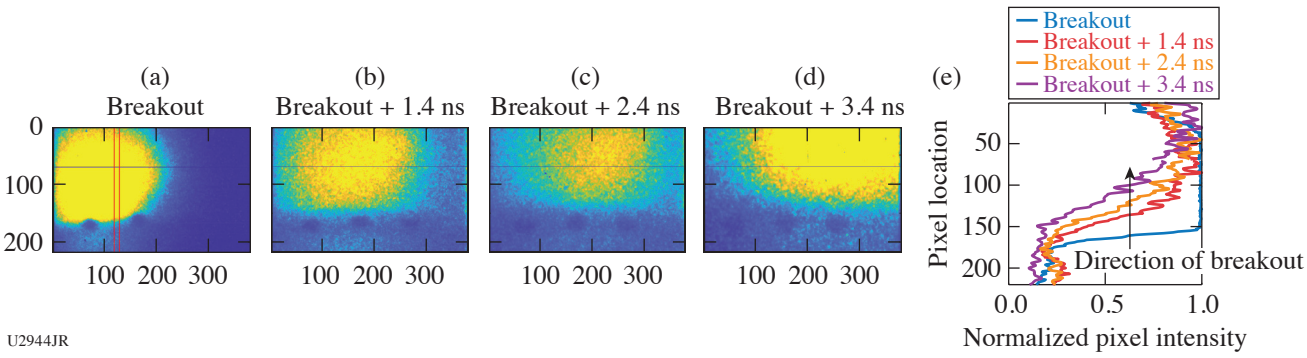

Figure 29
(a–d) Radiographs of the apex of a thin hemispherical plastic shell embedded with three titanium spherical particles (45-μm diameter, dark bodies) during and after shock breakout. The rarefaction wave travels from the bottom to the top of the image. The particles initially compress, and after 2.4 ns, appear to expand with the rarefaction wave. (e) Lineouts of normal pixel intensity in the area between two of the particles, outlined in the breakout image in red.

A qualitative analysis of the radiographs appears to show that the density gradient of the plasma decreases over time as the trailing edge of the rarefaction wave propagates into the vacuum. Further analysis is needed to determine if this is consistent with the angular filter refractometry data.

The experiment was conducted at the Omega Laser Facility at the University of Rochester's Laboratory for Laser Energetics with beam time through NLUF Program. This work was supported by the Department of Energy National Nuclear Security Administration under awards DE-SC0019329 and DE-NA0003914. Partial support from grants NSF PHY-2020249 and DE-SC0020229 and DE-NA0003914 is also acknowledged.

Rayleigh–Taylor Evolution of Isolated-Feature Perturbations in a Background Magnetic Field

B. Srinivasan,[1*] C. Samulski,[1] M. J.-E. Manuel,[2] and P. M. Nilson[3]
[1]Kevin T. Crofton Department of Aerospace and Ocean Engineering, Virginia Tech
[2]General Atomics
[3]Laboratory for Laser Energetics, University of Rochester
[*]Principal Investigator

The project aims to study magnetic-field effects on the Rayleigh–Taylor (RT) evolution of single-feature perturbations, such as those that exist in fill tubes, and to validate modeling which predicts reduced mix-width growth in the presence of magnetic fields. To achieve this, we developed a magnetized, shock-tube platform to study blast-wave–driven RT growth using the Fresnel zone plate (FZP) diagnostic.

On the first shot day, we tested the newly developed platform to explore whether the unmagnetized RT growth is detectable using the FZP diagnostic for two targets with different single-feature perturbations that were predicted to have significantly different evolution from simulations. We executed seven shots for the two targets by varying the timing of the diagnostic (0 ns, 3.5 ns, 5 ns, and 8 ns) to capture different stages of the RT evolution for each of the targets. Some raw FZP data from the shots are included to show a comparison between the two targets with different single-feature perturbations, where Fig. 30(a) is at 3.5 ns and Fig. 30(b) is at 5 ns.

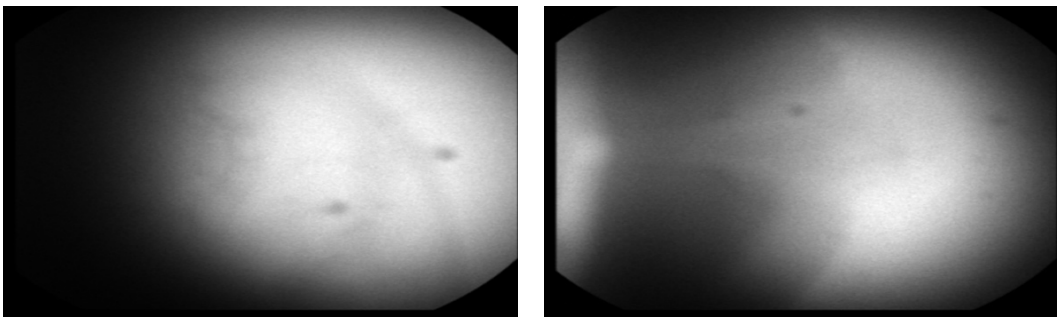

U2945JR

Figure 30
A quick analysis of the FZP images shows that (a) has multiple forks occurring with RT growth, whereas (b) has a more-uniform bubble growth, which is consistent with predictions from simulation.

Early analysis shows that our timing prediction from simulations needs a little refinement but there is generally good agreement of RT features between simulations and experiments. The features, however, were not captured with sufficient contrast to be clear and easily diagnosable for early and late times. These lessons are being applied toward the second shot day where further analysis is in progress to refine the timing in the simulations to improve the predictive capability. Additionally, the target is being redesigned due to the need for better contrast when using the FZP diagnostic. This was a successful shot day because it tested a new platform and provided very useful and relevant information to prepare for upcoming magnetized shots.

This work was supported by the DOE Office of Science under award number DE-SC0022319 and the NLUF Program for awarding and supporting the targets and the shot days.

Control of Laser–Plasma Interactions in Three-Dimensional–Printed Foam Structures with Graded Density

S. Tochitsky,[1*] N. Lemos,[2*] R. Simpson,[2] F. Fiuza,[3] A. Haid,[4] A. Pak,[2] D. Haberberger,[5] and C. Joshi[1]
[1]University of California, Los Angeles
[2]Lawrence Livermore National Laboratory
[3]Stanford Linear Accelerator Center
[4]General Atomics
[5]Laboratory for Laser Energetics, University of Rochester
[*]Principal Investigators

This work aimed to explore, through experiments and simulations, how laser-driven ion acceleration in a near-critical-density 3-D–printed target can be controlled by tailoring its density profile. We measured an enhancement up to 30%±20% of the maximum proton energy supported by a hotter electron distribution using a 3-D–printed target when compared with a simple 2-μm CH foil.

Intense research is being conducted into sources of laser-accelerated ions around the world (see e.g., a review by Macchi *et al*.[57] and the references therein). It is known that interactions of high-intensity lasers with solid-density targets can accelerate ion beams to tens of MeV/u by a well-studied target normal sheath acceleration (TNSA) mechanism or TNSA enhanced via radiation-induced transparency,[58,59] so-called breakout afterburner mechanisms.[60] Efforts to increase the maximum ion energy have largely focused on the development of novel acceleration mechanisms relying on ultrathin ($\leq$100-nm) targets that require utilization of single or double plasma mirrors to mitigate the effect of the laser prepulse to provide target survival. In this study we used special 3-D–printed targets in order to optimize the plasma density profile to maximize the laser absorption and proton/ion acceleration and minimize the sensitivity to laser prepulse. With the new 3-D printing technology, it is possible to fabricate complex structures with unprecedented geometric detail. Figure 31 shows an example of the targets that were fabricated by the General Atomics team who collaborated with us on the project and used this work as an opportunity to advance resolution of 3-D printing technology and metrology. We tested targets with different density gradients and maximum densities on the front and back surfaces, as well as targets with log-pile and stochastic low-density structures with densities in the range of 10^{20} to 10^{22} cm^{-3}.

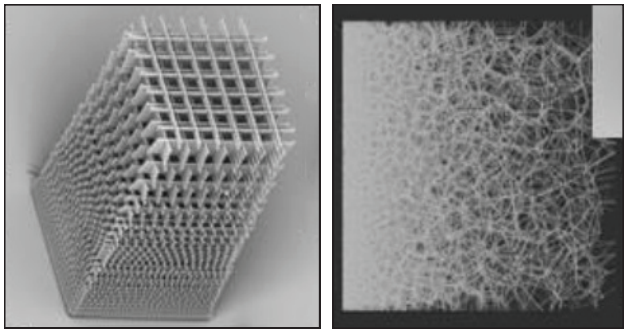

U2948JR

Figure 31
Examples of (a) a 3-D–printed log pile and (b) stochastic foam structure with graded density.

These targets were irradiated by the OMEGA EP laser with a pulse duration of 1 ps and maximum energy of 500 J. The spectrum of accelerated protons was measured using a Thomson parabola and a radiochromic film stack developed at LLNL (PROBIES). As a baseline, we used a 2-μm CH target that accelerated protons up to ~60 MeV from TNSA. Preliminary results show that an optimized 3-D–printed density profile target can accelerate protons up to at least 80-MeV energies. There targets showed good reproducibility that was relatively independent of the laser prepulse. Moreover, the log-pile targets seem to produce higher-energy protons than the stochastic targets.

Support by DOE Office of Science Early Career Research Program (Fusion Energy Sciences) under DOE-SC FWP 1651 and NNSA grant DE-NA0003842.

Dynamic Compression of Iron Carbide at Exoplanetary Core Conditions

S. J. Tracy,[1*] D. Kim,[1] S. Takagi,[1] I. I. Oleynik,[2] R. F. Smith,[3] F. Coppari,[3] M. Millot,[3] S. M. Clarke,[3] and J. H. Eggert[3]
[1]Carnegie Institution for Science
[2]University of South Florida
[3]Lawrence Livermore National Laboratory
[*]Principal Investigator

Our major scientific goal was to investigate the stable crystal structure of iron carbide (Fe_3C) at the pressure–temperature conditions of planetary cores. These results are highly sought after to establish improved models of structure, formation, and evolution of the cores of Earth and carbon-rich exoplanets. During our first shot day in September 2022, we utilized the unique capabilities of OMEGA EP to load Fe_3C samples along the principal isentrope to pressures between 250 and 600 GPa using a 10-ns ramped pulse. The compressed samples were probed with x-ray diffraction using the PXRDIP diagnostic [Fig. 32(d)][61] and pressures were determined using the ASBO diagnostic [Fig. 32(a)].[62] Figure 32 shows preliminary results for shot 37643 with a probe stress of 380 GPa. Early analysis of our results reveals that the orthorhombic Fe_3C structure is stable up to 600 GPa, placing new constraints on the Fe_3C phase diagram and equation of state.

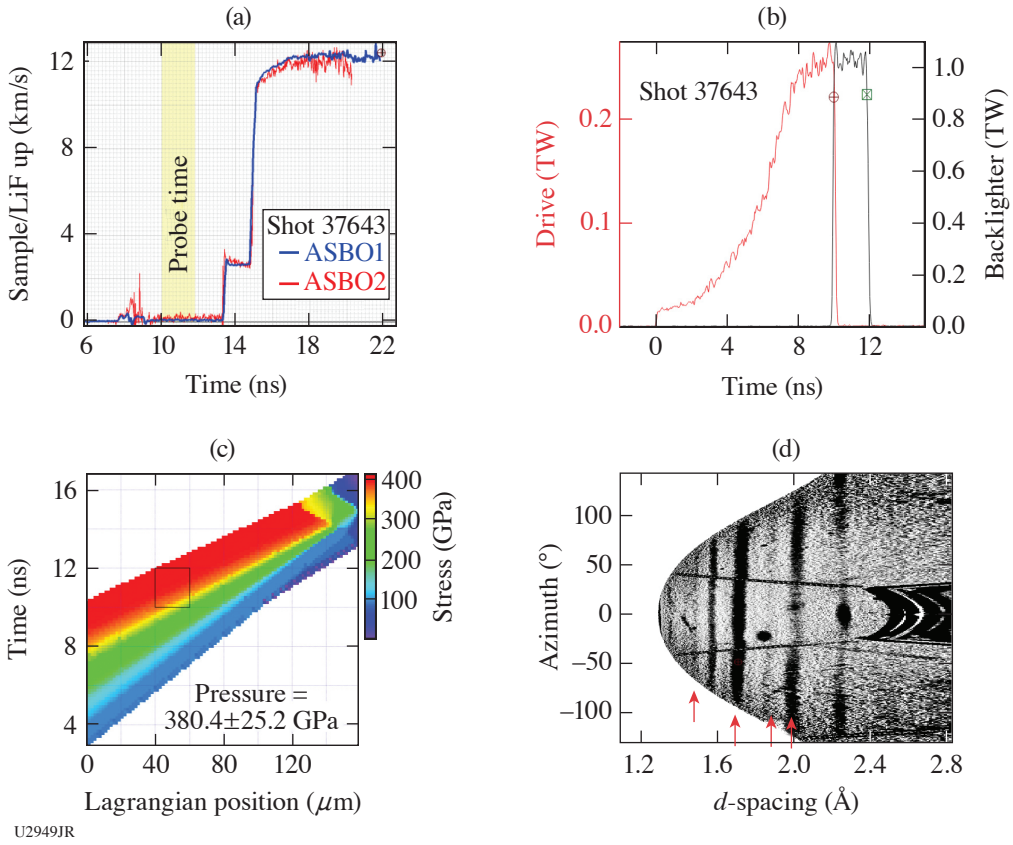

Figure 32
Preliminary analysis of results from shot 37643 for Fe_3C ramp compressed to a peak stress of 380 GPa. (a) VISAR data, Fe_3C–LiF interface velocity with 2-ns x-ray probe time in the yellow band. (b) Drive laser pulse (red trace). X rays are generated using a 2-ns square pulse (black trace). (c) Preliminary analysis of VISAR data showing a calculated map of stress distribution within the target assembly as a function of time. (d) De-warped x-ray diffraction data image plates with red arrows indicating compressed Fe_3C peaks.

The research is supported by the Department of Energy National Nuclear Security Administration under Award No. NA0004089.

Monochromatic Talbot–Lau X-Ray Deflectometer for the OMEGA EP and Multi-Terawatt Lasers

M. P. Valdivia[1,2*] C. Stoeckl,[3] T. Filkins,[3] C. Mileham,[3] M. Romanofsky,[3] I. A. Begishev,[3] V. Bouffetier,[4] G. Perez-Callejo,[5] A. Casner,[6] and D. Stutman[2,7]
[1]Center for Energy Research, University of California, San Diego
[2]Department of Physics and Astronomy, The Johns Hopkins University
[3]Laboratory for Laser Energetics, University of Rochester
[4]European XFEL GmbH, Germany
[5]Departamento de Física Teórica, Atómica y Óptica, Universidad de Valladolid, Spain
[6]CEA-CESTA, France
[7]ELI-NP, Institute for Physics and Nuclear Engineering, Romania
[*]Principal Investigator

The accurate diagnostic of density profiles in high-energy-density physics (HEDP) is an important but challenging task due to the high densities, small spatial scales, and short time scales encountered. In FY22, monochromatic 8-keV Talbot–Lau x-ray interferometry diagnostic capabilities were established for the OMEGA EP and Multi-Terawatt (MTW) lasers to increase HEDP phase-contrast diagnostic accuracy. Laterally graded multilayer mirrors were integrated to the design and the Talbot–Lau x-ray deflectometry (TXD) technique was improved based on previous results.[63] A new on-site x-ray calibration station reproduced vacuum chamber geometry, allowing for reliable instrument alignment. Preliminary experiments on MTW determined laser and target conditions, leading to optimal x-ray backlighter production for the 8-keV TXD (Table III). Additionally, a dedicated interferometry analysis code with a post-processing module was developed, delivering x-ray transmission, phase, and dark-field maps from moiré images.[64] Electron density retrieval methods were further enhanced by integrating phase-stepping capabilities to the analysis tool, making it possible to record *ex-situ* reference images on-site using the x-ray station in combination with x-ray backlighting from a copper x-ray tube.[65]

Monochromatic TXD (M-TXD) achieves high contrast (21% to 30%) close to the theoretical value (35%) for this configuration. Even with lower relative x-ray charge-coupled–device (CCD) counts, the signal-to-noise ratio (SNR) nearly doubles that of standard TXD, proving that monochromatic TXD successfully selects 8-keV contribution from Cu K_α emission, improving diagnostic performance by increasing electron density retrieval accuracy. Previously, alternative backlighter target configurations enhanced spatial resolution, albeit at the cost of reduced moiré fringe contrast due to increased high-energy emission (>8 keV) from hot-electron recirculation.[66] Therefore, x-ray backlighter quality from Cu wire targets and planar foils irradiated normal to the surface [i.e., edge-on from the TXD diagnostic line of sight (LOS)] and at standard 50° was evaluated for M-TXD.

Table III: Monochromatic TXD parameters for three MTW laser pulse lengths and standard TXD parameters for a matching laser pulse length.

Laser pulse length (ps)	Laser Intensity ($\times 10^{14}$ W/cm^2)	SNR	Contrast (%)	Relative CCD counts
25 (at 27 J)	7.3	6.0 to 7.9	24 to 25	1.00
60 (at 36 J)	4.1	6.9 to 7.2	21 to 24	1.30
80 (at 29 J)	2.5	6.0 to 8.6	27 to 30	0.71
Standard TXD				
24 (at 27 J)	4.4	3.5	19	1.85

Figure 33 shows M-TXD moiré images recorded using x-ray backlighting from Cu foil and wire targets irradiated at $I \sim 4 \times 10^{14}$ W/cm^2. Foils irradiated at 50° delivered a moiré fringe contrast of 24% and 6.9 SNR compared to a Cu wire contrast of 11% and 1.9 SNR for similar detector counts. Considering a Cu K_α conversion efficiency (CE) of $\sim 3 \times 10^{-5}$ for foils and $\sim 9 \times 10^{-6}$ for wires, it can be concluded that an overall photon count increase (higher laser intensity) could improve performance of wire x-ray backlighters, although additional data are needed to better determine their suitability for M-TXD diagnostics. Meanwhile, foils irradiated at 90° delivered 7% contrast and 1.2 SNR with reduced detector counts (~20%), which are inconsistent with CE measure-

ments. Lower photon counts can be attributed to diagnostic LOS and target misalignment, as observed on selected 50° foil shots. In the M-TXD configuration, a mirror alignment precision of ∼0.015° is required, which translates to extremely sensitive backlighter target and diagnostic LOS alignment. While x-ray emission from foils irradiated at 50° propagate toward the mirror unobstructed at 90°, x rays are obstructed by the foil itself. Since MTW's laser intensity was varied by displacing the target away from the laser focal spot, foils irradiated at 90° (edge-on to diagnostic) are most sensitive to alignment since the foil is displaced away from the mirror surface. Moreover, if the emission is highly directional, the total x rays reflected by the mirror would be further reduced. In turn, wire targets are less affected since the laser spot size is larger than their diameter and total x-ray emission is limited by the amount of material irradiated along the wire length. Consistent with the results shown, high moiré fringe contrast was measured (27% to 30%) for laser incidence angles of 50°, 70°, and 80° with similar detector photon counts. Respective spatial resolutions of ∼10.1 μm, ∼7.6 μm, and ∼5.6 μm, were measured with a 5.5-μm effective detector pixel size. Thus, 80° irradiation is an adequate compromise between spatial resolution and x-ray flux optimization, as is supported by previous results obtained in FY21.

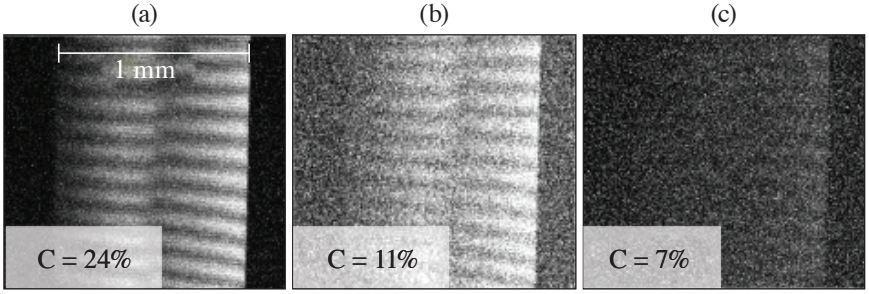

Figure 33
M-TXD moiré from Cu targets irradiated at $I \sim 4 \times 10^{14}$ W/cm^2: (a) foil at 50° from surface, (b) wire, and (c) foil at 90°. *The field of view is restricted due to mirror length. Contrast was enhanced to better showcase fringes. "Broken fringes" (middle of image) are due to grating imperfections.[67]

A 500-μm-diam CH rod was probed with M-TXD by laser irradiating ($I \sim 3 \times 10^{14}$ W/cm^2) foils at 50° (Fig. 34). The moiré images were analyzed with the newly developed Talbot numerical tool (TNT). Matching reference images were not available through experimental acquisition or *ex-situ* phase-stepping methods, hence, a reference was selected from images recorded with different laser parameters through correlation. Phase retrieval was enabled by the backlighter background removal feature included in TNT, included in consideration of data acquisition limitations encountered in most HEDP experiments. The feature allows for postprocessing using reference images recorded with different x-ray sources, which is a powerful resource for TXD diagnostics. Figure 34(d) shows the x-ray refraction angle profile retrieved with TNT (yellow). The G0 source grating background refraction profile (purple curve), obtained from the reference image and a flat field background reveals the grating structure imperfections that contribute to the overall x-ray refraction profile retrieved with TNT. In this case, grating imperfections are significant enough to prevent accurate phase retrieval in the "broken" fringe section. Nevertheless, outside this area, the x-ray refraction angle profile matches simulations within experimental error. Note that *IDEA*, a standard phase-retrieval code, could not deliver a phase map using this input, which proves TNT is a valuable advancement for TXD diagnostic techniques.

An NLUF OMEGA EP campaign was performed in FY22Q4. Multiple factors contributed to a total lack of M-TXD data. Ground vibrations due to building construction and imprecise source grating target fabrication/mounting affected M-TXD rail alignment. Laser beam source failure delayed shots and persistent x-ray CCD data acquisition failures, along with incorrect mounting of a collimator plate, caused further delays and data loss. Improvements and procedure changes have been made in response to these issues where appropriate. Note that x-ray backlighter spectral data were successfully acquired and will be used to complement data from previous campaigns, which will be the subject of a future publication. Further, in preparation for a second NLUF shot (FY23Q2), additional measures have been taken to ensure proper diagnostic performance. The previous OMEGA EP campaign goals to determine laser parameters for optimal x-ray backlighter considering moiré fringe contrast and spatial resolution will be pursued.

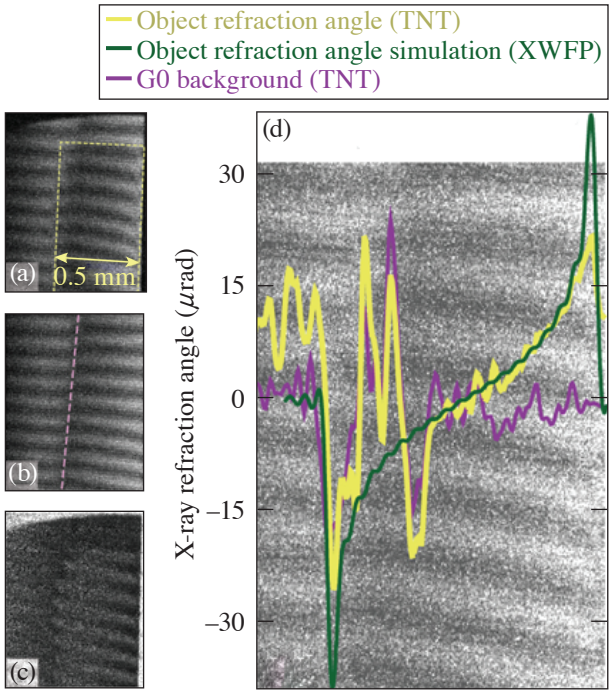

Figure 34
(a) CH rod moiré (yellow line) recorded with an ~36-J, 70-ps laser pulse. (b) Reference moiré from a 36-J, 60-ps laser pulse. The pink line marks grating imperfections. (c) Differential object/reference image. (d) X-ray refraction angle profile from TNT, simulations, and reference "background." XWFP: X-ray wavefront propagation.

This work was supported by NNSA Grant HEDLP DE-NA0003882. OMEGA EP laser beam time was awarded through NLUF by the University of Rochester's Laboratory for Laser Energetics under the auspices of the U.S. DOE/NNSA Contract DE-NA0003856.

Experimental Measurement of Thermal Conductivity in Warm Dense Matter

T. G. White,[1*] T. Doeppner,[2] C. H. Allen,[1] M. Oliver,[3] L. Divol,[2] A. Kemp,[2] E. Kemp,[2] O. Landen,[2] Y. Ping,[2] M. Schölmerich,[2] and W. Theobald[4]
[1]University of Nevada, Reno
[2]Lawrence Livermore National Laboratory
[3]Central Laser Facility, UK
[4]Laboratory for Laser Energetics, University of Rochester
[*]Principal Investigator

The thermal conductivity for materials at warm-dense-matter (WDM) conditions plays a vital role in planetary physics and ICF efforts. In the former, predictions of the power supplied by the geodynamo are utilized to constrain the Earth's evolution, while in the latter, heat transport between the layers plays an essential role in capsule implosions. As is typical for transport properties in the warm-dense-matter regime, however, a dearth of experimental measurements has led to a considerable body of theoretical and computational work that exhibit significant differences.

At the interface between two materials, initially at different temperatures, slow thermal conduction combined with rapid pressure equilibration produces gradients in the density profile on either side of the interface. On a nanosecond time scale, these density gradients typically have scale lengths of the order of 1 μm. We have developed a radiography platform for OMEGA that uses thin slits cut with a focused ion beam to perform micron-scale radiography—the highest spatial resolution achieved to date. Furthermore, due to the partially spatially coherent source, we observe significant diffractive and refractive effects in the radiograph; therefore, the technique is termed Fresnel diffractive radiography.

Initial data taken using plastic-coated tungsten wires are shown in Fig. 35. The data taken at 0 ns (i.e., no drive lasers) provided a measurement of the platform resolution,[68,69] which is less than 2 μm. A time sequence of the wire evolution after the drive was obtained, where we clearly see the outgoing shock wave launched from the expanding tungsten and the rarefaction wave traveling inward from the outside of the cylinder, both of which can be used to constrain the material equation of state and deposited energy. Most importantly, the high-resolution radiography captured information at the interface, with a well-characterized diffraction pattern observed in the 4-ns data at ~12 μm.

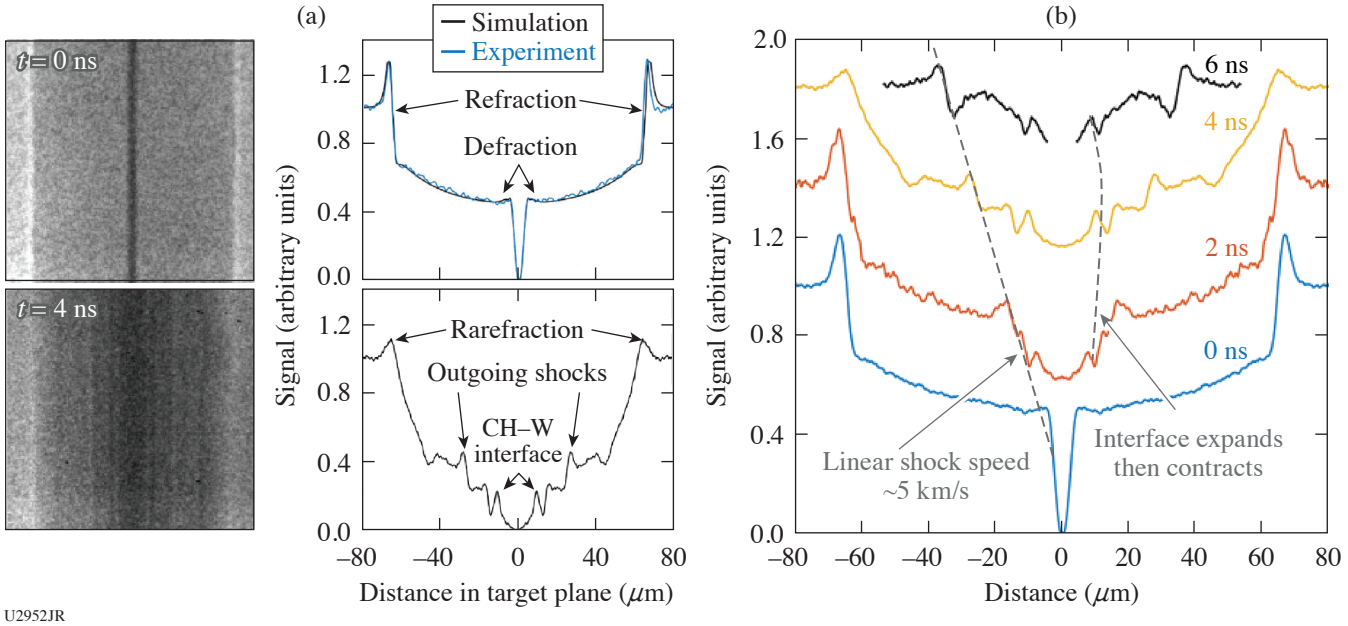

Figure 35
(a) Radiographs and lineouts of a cold target (top) and a driven target (bottom). A clear change in the features is evident in the lineouts, showing the expanded W–CH interface, as well as shock waves launched into the CH. (b) A plot showing the time evolution of our data over the course of the experiment. The signal lineouts are spread out vertically to better see the changes. The shock trajectory and interface evolution are highlighted by the dashed lines.

To analyze the driven data, we solve the Fresnel–Kirchoff integral[70] for a synthetic density profile, incorporating a parameterized material interface to resolve the features we see in the data. Specifically, we expect to see a discontinuity at the interface with a density slope on either side. As seen in Fig. 36, our simulated density profile reproduces the experimental diffraction pattern exceptionally well. We note, however, that the shock is additionally blurred in the experimental data due to its high velocity and the 250-ps gate time of the framing camera. We use Bayesian inference to sample parameter space to better constrain our results and provide error estimates. From this we have extracted the density scale lengths in each material, approximately 0.9±0.15 μm for the tungsten and 1.6±0.3 μm for the plastic.

In these initial experiments, we used tungsten wires due it the high opacity. However, we have now changed from plastic-coated tungsten to plastic-coated nickel and copper wires since as these materials are of broader interest. We are still in the process of analyzing the results and are simultaneously working to improve the platform for our next shot day. Thus far, this work has resulted in two publications (see Refs. 68 and 69). In addition, we are currently working toward a publication on our thermal conductivity measurement.

This work has been supported by the National Science Foundation under Grant No. PHY-2045718. The work of T. Doeppner, L. Divol, A. Kemp, E. Kemp, O. Landen, Y. Ping, and M. Schölmerich was performed under the auspices of the U.S. Department of Energy by Lawrence Livermore National Laboratory under Contract DE-AC52-07NA27344 and supported by Laboratory Directed Research and Development (LDRD) Grant No. 21-ERD-029.

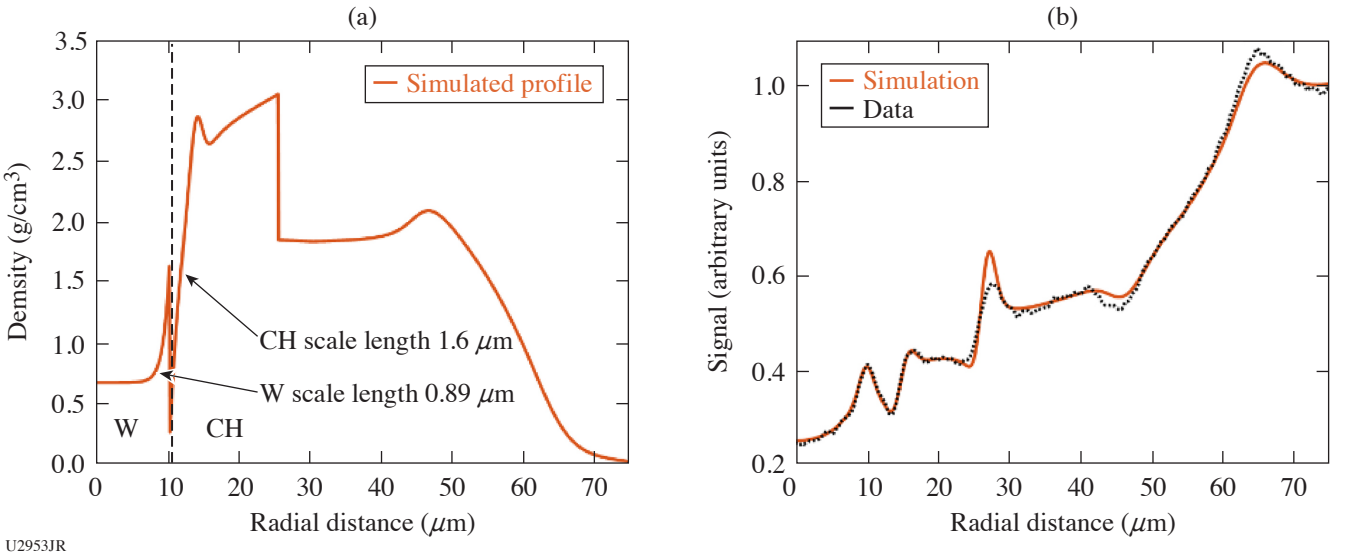

Figure 36
(a) Simulated radial density profiles that we have created to match our data, with a discontinuity at the interface, the outward-traveling shock wave, and the rarefaction of the outer plastic edge. The material interface is located at a radius of around 10 μm. The measured scale lengths of each material's density profile are given. (b) The simulated diffraction pattern from the density profile given in (a) is compared with the data at 4 ns from above. We see excellent fitting, especially in the region near the material interface at 10 μm. The shock wave at 27 μm has not considered any motion blurring, and as such diverges from the data.

Relativistic Intensity Laser Channeling and Direct Laser Acceleration of Electrons from an Underdense Plasma

H. Tang,[1] I.-L. Yeh,[2] P. T. Campbell,[1] F. Albert,[3] H. Chen,[3] Y. Ma,[1] A. McKelvey,[1] P. M. Nilson,[4] B. K. Russell,[1] J. L. Shaw,[4] A. G. R. Thomas,[1] A. V. Arefiev,[2] and L. Willingale[1*]
[1]University of Michigan
[2]University of California, San Diego
[3]Lawrence Livermore National Laboratory
[4]Laboratory for Laser Energetics, University of Rochester
[*]Principal Investigator

Laser–plasma interactions generate high-energy electrons, which have a number of potential applications, including generating secondary sources like bright x-ray radiation, electron–positron pairs, ion acceleration, or neutron generation. The direct laser acceleration (DLA) mechanism uses the laser's electric field, in the presence of an external field such as the channel fields, to produce a relativistic electron beam. Our experiments aim to understand the DLA dynamics and optimize the high-energy electron beam production. The experimental variables are plasma density, laser pulse duration, focusing geometry, and laser energy. For the FY22 shots, expanded the parameter space was explored, building on previous data; the secondary x-ray emission using a Ross pair filter was also investigated.

The apodized backlighter laser pulse was focused onto the edge of a 2-mm-diam helium gas-jet target with a plasma density of either $0.01n_c$ or $0.004n_c$, where n_c is the critical density. An *f*/5 apodizer was utilized for most shots. The laser energy was decreased from 110 J to 12 J to observe the acceleration mechanism in low a_0 regime. We also performed one shot using an *f*/8 apodizer to study the effect of a large beam. In order to study the effect of laser pulse duration on laser channeling, we used a 3-ps pulse for our final shot. The main diagnostics were EPPS3 Rad (electron–positron–proton spectrometer) and proton radiography, which employed the sidelighter beam, and a 50-μm Cu foil to generate the proton beam. Additionally, the 4ω probe was turned on, taking shadowgraphy and angular filter refractometry data to observe the channel.

As shown in Fig. 37(a), the proton radiography imaged the laser channel structure after a 3-ps laser pulse propagation through the gas column from left to right. The channel walls generate a bump in the center of the picture, implying the formation of

new laser modes when the laser travels through the plasma. The dark line segment inside the channel (shown by orange arrow) indicates the field reversal, which is due to the ion motion. Figure 37(b) shows the electron spectra. Electrons with energy up to 170 MeV were observed. The effective temperature decreases with the laser energy for a fixed laser focal spot size. Figure 37(c) shows the Ross pair filters and a raw image of the x ray on an image plate. The x-ray diagnostic was installed behind the EPPS. The Ross pair filters contain eight sections, which are made by different metal materials with varying thicknesses. A hole was on the back of the filter; therefore, eight small sections blocked the x ray with different cutoff energies, forming a round disk with eight sections of different brightnesses. A rough analysis estimated the x-ray energy to be in the 10- to 100-KeV range. Further calculation and calibration need to be performed for x-ray measurement.

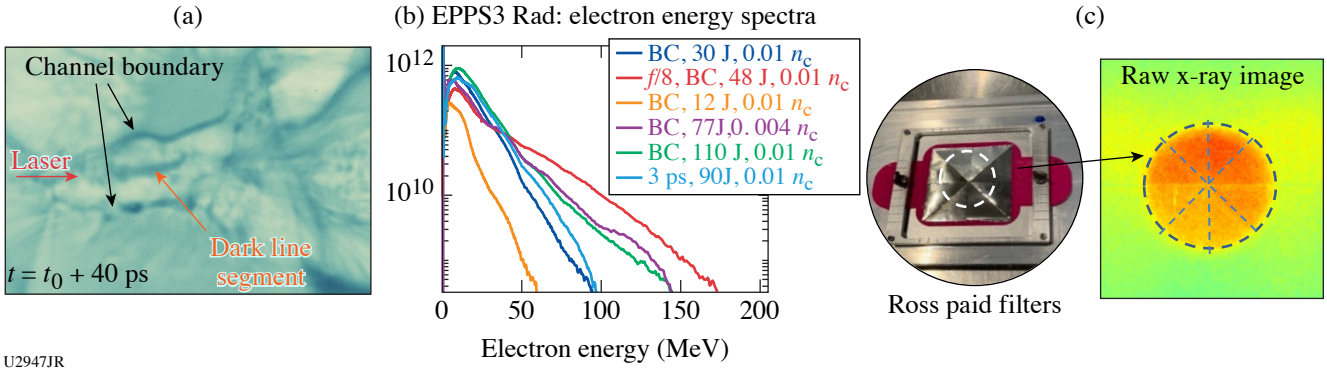

Figure 37
(a) Raw proton radiography image from shot 37147. The red arrow represents the laser propagation direction, the black arrows point at the channel walls, and the orange arrow points at the dark line segment inside the channel. The image was taken 40 ps after the interaction. (b) Electron spectra from the 16 June 2022 shot day. (c) Ross pair filters and raw x-ray image from shot 37147.

This material is based upon work supported by the Department of Energy/NNSA under Award Number DE-NA0004030.

1. K. Bhutwala *et al.*, Phys. Rev. E **105**, 055206 (2022).
2. C. McGuffey *et al.*, Bull. Am. Phys. Soc. **65**, VO05.00005 (2020).
3. J. Saret *et al.*, "Measurements of Temperature Evolution in Copper from Intense Proton Beam Energy Deposition," in preparation.
4. C. McGuffey *et al.*, Sci. Rep. **10**, 9415 (2020).
5. W. Fox, A. Bhattacharjee, and K. Germaschewski, Phys. Rev. Lett. **106**, 215003 (2011).
6. W. Fox *et al.*, submitted to Physical Review Letters, available arXiv:2003.06351 (2020).
7. C. L. Johnson *et al.*, Rev. Sci. Instrum. **93**, 023502 (2022).
8. A. F. A. Bott *et al.*, J. Plasma Phys. **83**, 905830614 (2017).
9. S. Zhang *et al.*, "Ion and Electron Acoustic Bursts During Anti-Parallel Reconnection Driven by Lasers," to be published in Nature Physics.
10. L. Gao *et al.*, Phys. Plasmas **23**, 043106 (2016).
11. A. Chien *et al.*, Phys. Plasmas **26**, 062113 (2019).
12. A. Chien *et al.*, Phys. Plasmas **28**, 052105 (2021).
13. K. D. Meaney, presented at the 64th Annual Meeting of the APS Division of Plasma Physics, Spokane, WA, 17–21 October 2022 (YI01.00002).
14. B. J. Winjum, F. S. Tsung, and W. B. Mori, Phys. Rev. E **98**, 043208 (2018).
15. M. Bailly-Grandvaux *et al.*, J. Plasma Phys. **89**, 175890201 (2023).
16. B. J. Winjum *et al.*, Phys. Rev. Lett. **110**, 165001 (2013).
17. X. Sha *et al.*, Sci. Rep. **5**, 11003 (2015).
18. H. Liu, J. S. Tse, and H. Mao, J. Appl. Phys. **100**, 093509 (2006).

19. J. E. Jaffe *et al.*, Phys. Rev. B **62**, 1660 (2000).
20. Z. Li *et al.*, Phys. Rev. B **79**, 193201 (2009).
21 N. V. Kabadi *et al.*, Phys. Rev. E **104**, L013201 (2021).
22. M. J. Rosenberg *et al.*, Phys. Rev. Lett. **112**, 185001 (2014).
23. H. Sio *et al.*, Rev. Sci. Instrum. **87**, 11D701 (2016).
24. B. Reichelt *et al.*, Bull. Am. Phys. Soc. **66**, UO04.00006 (2021).
25. M. Gatu Johnson *et al.*, Phys. Plasmas **27**, 032704 (2020).
26. S. Brygoo *et al.*, Nature **593**, 517 (2021).
27. P. M. Nilson *et al.*, Phys. Rev. Lett. **97**, 255001 (2006).
28. R. Samtaney *et al.*, Phys. Rev. Lett. **103**, 105004 (2009).
29. E. Greco *et al.*, Astrophys. J. Lett. **908**, L45 (2021).
30. J. E. Gudmundsson, C. J. Pethick, and R. I. Epstein, Astrophys. J. **272**, 286 (1983).
31. S. D. Bergeson *et al.*, Phys. Plasmas **26**, 100501 (2019).
32. B. Strömgren, Astrophys. J. **89**, 526 (1939).
33. R. P. Drake *et al.*, Astrophys. J. **833**, 249 (2016).
34. A. Mizuta *et al.*, Astrophys. J. **621**, 803 (2005).
35. A. M. Hansen *et al.*, Rev. Sci. Instrum. **89**, 10C103 (2018).
36. E. N. Parker, *Cosmical Magnetic Fields: Their Origin and Their Activity*, The International Series of Monographs on Physics (Clarendon Press, Oxford, 1979).
37. B. Fryxell *et al.*, Astrophys. J. Suppl. Ser. **131**, 273 (2000).
38. P. Tzeferacos *et al.*, High Energy Density Phys. **17**, 24 (2015).
39. P. Tzeferacos *et al.*, Phys. Plasmas **24**, 041404 (2017).
40. P. Tzeferacos *et al.*, Nat. Commun. **9**, 591 (2018).
41. *2019 John Dawson Award for Excellence in Plasma Physics Research Recipient*, Petros Tzeferacos, University of Chicago, (2019).
42. A. F. A. Bott *et al.*, Proc. Natl. Acad. Sci. **118**, e2015729118 (2021).
43. A. F. A. Bott *et al.*, Matter Radiat. Extremes **7**, 046901 (2022).
44. L. E. Chen *et al.*, Astrophys. J. **892**, 114 (2020).
45. J. Meinecke *et al.*, Sci. Adv. **8**, eabj6799 (2022).
46. A.F. A. Bott *et al.*, Phys. Rev. Lett. **127**, 175002 (2021).
47. A. Kolmogorov, Dokl. Akad. Nauk SSSR **30**, 301 (1941).
48. L. Gao *et al.*, Astrophys. J. Lett. **873**, L11 (2019).
49. Y. Lu *et al.*, Phys. Plasmas **26**, 022902 (2019).
50. Z. He *et al.*, Sci. Adv. **8**, eabo0617 (2022).
51. D. Kraus *et al.*, Nat. Astron. **1**, 606 (2017).
52. M. C. Marshall *et al.*, J. Appl. Phys. **131**, 085904 (2022).
53. R. F. Smith *et al.*, J. Appl. Phys. **131**, 245901 (2022).
54. R. F. Smith *et al.*, Nature **511**, 330 (2014).
55. P. K. Patel *et al.*, Phys. Rev. Lett. **91**, 125004 (2003).
56. D. Haberberger *et al.*, Phys. Rev. Lett. **123**, 235001 (2019).
57. A. Macchi, M. Borghesi, and M. Passoni, Rev. Mod. Phys. **85**, 751 (2013).
58. S. Palaniyappan *et al.*, Nat. Commun. **6**, 10170 (2015).
59. A. Higginson *et al.*, Nat. Commun. **9**, 724 (2018).
60. L. Yin *et al.*, Phys. Rev. Lett. **107**, 045003 (2011).
61. J. R. Rygg *et al.*, Rev. Sci. Instrum. **83**, 113904 (2012).
62. P. M. Celliers *et al.*, Rev. Sci. Instrum. **75**, 4916 (2004).
63. M. P. Valdivia *et al.*, Rev. Sci. Instrum. **92**, 065110 (2021).
64. G. Pérez-Callejo *et al.*, Phys. Plasmas **29**, 043901 (2022).

65. G. Pérez-Callejo *et al.*, "Phase Imaging of Irradiated Foils at the OMEGA EP Facility Using Phase-Stepping X-Ray Talbot–Lau Interferometry," in preparation.
66. M. P. Valdivia *et al.*, Rev. Sci. Instrum. **89**, 10G127 (2018).
67. M. P. Valdivia, D. Stutman, and M. Finkenthal, Rev. Sci. Instrum. **85**, 073702 (2014).
68. C. H. Allen *et al.*, Appl. Opt. **61**, 1987 (2022).
69. M. Oliver *et al.*, Rev. Sci. Instrum. **93**, 093502 (2022).
70. A. Pogany, D. Gao, and S. W. Wilkins, Rev. Sci. Instrum. **68**, 2774 (1997).